UNIVERSITÄT
DUISBURG
ESSEN

Open-Minded

Bachelor thesis

Magnetic anisotropy of disordered neon-irradiated iron-rhodium thin films studied with ferromagnetic resonance

Name: Jonas Wiemeler

Major: Physics B. Sc.

Date of submission: 26.08.2019

Supervisor: Prof. Dr. rer. nat. Michael Farle

Contents

1. Motivation **1**

2. Theoretical Background **2**
2.1. Magnetic anisotropy . . . 2
2.1.1. Free Energy Density . . . 2
2.1.2. Shape Anisotropy . . . 3
2.1.3. Magnetocrystalline anisotropy . . . 3
2.2. Magnetisation Dynamics . . . 5
2.3. Ferromagnetic Resonance / FMR . . . 6

3. Methods **8**
3.1. Measurement Setup . . . 8
3.1.1. Electron Paramagnetic Resonance / FMR Spectrometer . . . 8
3.1.2. FMR and EPR signal line shape . . . 9
3.1.3. Angular dependence setup for FMR measurements . . . 10
3.2. FeRh thin films . . . 11
3.2.1. Preparation of FeRh thin films . . . 12
3.2.2. Properties of FeRh thin films . . . 13

4. Results and discussion **16**
4.1. Measurements of FeRh thin films with low fluence . . . 16
4.1.1. FeRh-1 . . . 16
4.1.2. FeRh-2 . . . 20
4.2. Measurements of FeRh thin films with moderate fluence . . . 23
4.2.1. FeRh-3 . . . 23
4.2.2. FeRh-4 . . . 27
4.3. Measurements of FeRh thin film with high fluence . . . 29
4.3.1. FeRh-5 . . . 29
4.3.2. FeRh-6 . . . 32
4.4. Analysis of the anisotropy of FeRh . . . 35

5. Conclusions and outlook **38**

A. Appendix **39**
A.1. Plots . . . 39
A.2. Free energy density/ potential landscape . . . 40
A.2.1. Uniaxial . . . 41
A.2.2. Cubic . . . 42
A.2.3. Free energy density for FeRh-2 . . . 43
A.3. Open questions . . . 43

1. Motivation

A binary FeRh alloy plays a significant role in the development of new technologies. For example, FeRh has a huge magnetocaloric effect (MCE) due to its first-order phase transition from antiferromagnetic to ferromagnetic phase at temperatures close to room temperature. Thus, FeRh would be a suitable material to develop magnetic cooling devices [1]. A disorder of the crystal lattice controlled by low energy ion irradiation allows to tune certain properties, such as magnetic anisotropy or phase transition temperature. The property of varying the critical temperature by structural disorder also could provide aplication in future storage media. Thus, the so-called Heat Assisted Memory Recording (HAMR) can be implemented using a FeRh/FePt bi-layer. Here, FePt with its high magneto-crystalline anisotropy serves as a memory for bits [2]. FeRh now makes it possible to lower the coercive field of FePt by a phase transition from antiferromagnetic to ferromangetic state, using thermal excitation. The ferromagnetic state serves here to increase the storage density, while the antiferromagnetic state ensures long-term storage. The ability to modify certain magnetic properties of FeRh thin films films via ion-beam irradiation and disorder opens new possibilities for further development of cooling devices as well as magnetic memory recording based on this alloy. The goal of this bachelor thesis is to investigate the magnetic anisotropy of differently disordered FeRh thin films with 40 nm thickness by means of the ferromagnetic resonance.

2. Theoretical Background

2.1. Magnetic anisotropy

2.1.1. Free Energy Density

The magnetic anisotropy can best be described with the Helmholtz free energy A and its density per volume F_{Ani} of a magnetic single domain system as a function of the direction of the magnetisation $\vec{m} = \frac{\vec{M}}{M}$. The magnetisation prefers the direction of minimal energy. This direction is called the easy axis, on the other hand the direction of maximal energy is called the hard axis. In order to deflect the magnetisation, $\vec{M}$, out of the easy direction, an external magnetic field is used to spend the work $\vec{f} \cdot \vec{B}_{Ext} \cdot d\vec{M}$ per volume, $d\vec{M}$ is the change of the magnetisation vector and $\vec{f}$ is the system's energy density [3].
The easy axis can now be used as the reference direction in order to define the Magnetic Anisotropy Energy (MAE) as the difference of the free energy density F of the easiest and the hardest direction. The work to deflect the magnetisation is given by the grand potential of thermodynamics Ω

$$\Omega = A - G, \tag{2.1}$$

here A is the Helmholtz free energy and G is the Gibbs free enthalpy [4].
For experiments it is easier to keep parameters such as temperature, pressure, tensions and others on a constant state, than it is keeping a constant volume.
In this case, the energy density is best described as the Gibbs free enthalpy density G_{Ani}. Assuming a constant pressure and the Zeeman-energy as the potential $\Omega = \vec{M} \cdot \vec{B}_{ext}$, the free enthalpy density G_{Ani} can be written as a function dependent of the free energy density F_{Ani} [4, 3].

$$G_{Ani} = F_{Ani} - \vec{M} \cdot \vec{B}_{ext} \tag{2.2}$$

There are two major contributions to the MAE, the dipole-dipole coupling and the spin-orbit interaction. As shown in Eq.(2.3) and Eq.(2.4) both energies contain spin and spatial coordinates, thus making the energy dependent of the relative orientation of the magnetic moment and the lattice. The exchange interaction in its Heisenberg form is isotropic. Only when considering different exchange constants along different crystallographic directions this energy can lead to a strong anisotropy, for example in oxides.
The Hamiltonian of the dipole-dipole coupling $\hat{H}_{dd}$ is:

$$\hat{H}_{dd} = \frac{1}{4\pi\epsilon_0} \frac{1}{|R^3_{i,j}|} \left[\vec{S}_i \cdot \vec{S}_j - \frac{3}{|R_{i,j}|^2} (\vec{S}_i \cdot \vec{R}_{i,j})(\vec{S}_j \cdot \vec{R}_{i,j}) \right] \tag{2.3}$$

where *i* and *j* are two different dipoles, $\vec{R}_{i,j}$ the connecting vector of the dipoles, $|\vec{R}_{i,j}|$ the distance between dipole *i* and dipole *j* and $S_{i,j}$ is the spin of particle *i,j* [5].
The Hamiltonian of the spin-orbit interaction is [5]:

$$\hat{H}_{LS} = -\lambda L_i \cdot S_i = -\frac{\mu_B}{\hbar m_e e c^2} \left(\frac{1}{r} \frac{dV}{dr} \right) L_j \cdot S_i \tag{2.4}$$

here $\lambda = \frac{\mu_B}{\hbar \mathrm{m}_e e \mathrm{c}^2}$ is the spin-orbit coupling constant, $\hat{\mathrm{H}}_{\mathrm{LS}}$ is the spin–orbit potential in an external electrostatic potential V, with *e* as the elementary charge, m_e is the mass of an electron, c is the speed of light, L is the angular momentum and S is the spin of an electron.

2.1.2. Shape Anisotropy

The macroscopic shape anisotropy is generated by the dipole-dipole coupling inside the sample and contributes to a preferred direction depending on the geometric shape of the sample. The shape anisotropy varies in different shapes, e.g. spheres, cubes, thin films, etc.
The dipole-dipole coupling is a long range effect, which spreads across the hole sample, including the interfaces. With Maxwell's equation of magnetostatics $\vec{\nabla} \cdot \vec{\mathrm{B}} = 0$, a surface polarisation is induced. This means a so-called demagnetizing field describes the part of the magnetic field which has the opposite polarisation as the macroscopic magnetisation. If the sample has a homogeneous magnetisation $\vec{\mathrm{M}}$, it applies,

$$\vec{\mathrm{B}}_{\mathrm{dem}} = \underline{\underline{\mathrm{N}}} \mu_0 \vec{M} \tag{2.5}$$

The demagnetising field is described by a demagnetizing tensor $\underline{\underline{\mathrm{N}}}$. The energy contribution of the dipole-dipole coupling can therefore be described as,

$$\mathrm{F}_{\mathrm{dd}} = \frac{1}{2} \mu_0 (\mathrm{N}_{\mathrm{x}} \mathrm{M}_{\mathrm{x}}^2 + \mathrm{N}_{\mathrm{y}} \mathrm{M}_{\mathrm{y}}^2 + \mathrm{N}_{\mathrm{z}} \mathrm{M}_{\mathrm{z}}^2) \tag{2.6}$$

If the sample is formed as a spheroid with a rotation around its c-axis, one obtains the simplification $\mathrm{N}_{\mathrm{x}} = \mathrm{N}_{\mathrm{y}} = \mathrm{N}_{\perp}$ and $\mathrm{N}_{\mathrm{z}} = \mathrm{N}_{\parallel}$, therefore Eq.(2.6) can be written as [6]

$$\mathrm{F}_{\mathrm{dd}} = \frac{1}{2} \mu_0 |\vec{\mathrm{M}}_{\mathrm{S}}|^2 (\mathrm{N}_{\perp} \cos^2(\theta) + \mathrm{N}_{\parallel} \sin^2(\theta)), \tag{2.7}$$

where $\mathrm{N}_{\perp}$ and $\mathrm{N}_{\parallel}$ are the demagnetizing factors in the appropriate direction. Since the studied samples are thin films, whose thickness is small compared to the overall dimensions, an electrostatic boundary problem has not been considered [6]. In this case the demagnetizing field reduces to $\mathrm{N}_{\perp} = 1$ and $\mathrm{N}_{\parallel} = 0$, the shape anisotropy is given by

$$\mathrm{F}_{\mathrm{dd}} = \frac{1}{2} \mu_0 |\vec{\mathrm{M}}_{\mathrm{S}}|^2 \cos^2(\theta) \tag{2.8}$$

In equation 2.8, there is a minimum energy at an angle of $\theta = \frac{\pi}{2}$. This is the preferred direction of the magnetisation, so called easy axis. A sample in which only the shape anisotropy exists would have an equilibrium magnetisation parallel to the surface. As one can see, this anisotropic energy heavily depends on the magnetisation, therefore the shape anisotropy of thin films with high saturation magnetisation $\vec{\mathrm{M}}_{\mathrm{S}}$ has a big contribution to the MAE.

2.1.3. Magnetocrystalline anisotropy

The crystalline anisotropy describes every anisotropic contribution, that depends on the crystalline symmetry. The main reason of the magnetocrystalline anisotropy is the spin–orbit (LS) interaction of the electrons of the atoms in the lattice, this can be described by the crystal field. The crystal field, which is an electric field generated by the lattice, has an influence on the orbital movement of the electrons. As a result, the LS-interaction couples the spin to the crystal

field. This creates a small additional orbital magnetism that affects the direction of spontaneous magnetisation [5].
To explain this phenomenon, it is advisable to look at the local surrounding of a single magnetic moment. The mathematical approach is to create a power series with respect to the local crystal symmetry, thus considering direction cosines relative to the crystal axes [6]. If the crystal has a cubic symmetry, one obtains

$$\mathrm{F_C} = \mathrm{K_4}(\alpha_1^2\alpha_2^2 + \alpha_2^2\alpha_3^2 + \alpha_3^2\alpha_2^2) + \mathrm{K_6}\alpha_1^2\alpha_2^2\alpha_3^2 \tag{2.9}$$

Here the $\alpha_i = \dfrac{\mathrm{M_i}}{\mathrm{M}}$ are the direction cosines of $\mathrm{M_S}$ with $\mathrm{M_i}$ as the projection of the magnetisation with respect to a crystal axis i and $\mathrm{K_4}$ and $\mathrm{K_6}$ are the first and the second order anisotropy constants, representing the first and second order of the cubic magnetocrystalline anisotropy.
For crystals with uniaxial symmetry, only the even powers are used, to obtain a symmetry which is present in the in-plane direction parallel to the outer magnetic field and to ensure that the energy is time-reversal invariant [7].

$$\mathrm{F_{Uni,\parallel}} = -\mathrm{K_{2\parallel}}\alpha_{\mathrm{x}}^2 = -\mathrm{K_{2\parallel}}\sin^2(\theta)\cos^2(\phi - \phi_{\mathrm{u}}) \tag{2.10}$$

Here ϕ_u is the easy axis in respect to crystal direction [100]. The numbers are now representing in how many directions the anisotropy is present. For example, the uniaxial symmetry takes place along one axis. Therefore it has contributions in two direction, one in the positive and one in the negative region. Furthermore they are divided into parallel $\parallel$ and perpendicular $\perp$, this allows a differentiation of in-plane and out-of-plane anisotropy in respect to the sample normal. A perpendicular uniaxial and cubic anisotropy is described by $\mathrm{K_{2\perp}}$ and $\mathrm{K_{4\perp}}$ [8].

$$\mathrm{F_{Uni,\perp}} = -\mathrm{K_{2\perp}}\alpha_3^2 - \mathrm{K_{4\perp}}\alpha_3^4 = \mathrm{K_{2\perp}}\sin^2(\theta) - \mathrm{K_{4\perp}}\cos^4(\theta) = \mathrm{K_{2\perp}}\sin^2(\theta) - \mathrm{K_{4\perp}}\cos^4(\theta) \tag{2.11}$$

If the sample is cubic but has a deformation, that one of the crystal lattice parameters in the unit cell is bigger or smaller, a tetragonal symmetry arises. Therefore, a tetragonal contribution F_{tet} needs to be considered. This may result in a preferred direction along the z-axis [8].

$$\begin{aligned}\mathrm{F_{tet}} &= \mathrm{K_{2\perp}}\alpha_3^2 + \frac{1}{2}\mathrm{K_{4\perp}}\alpha_3^4 + \frac{1}{2}\mathrm{K_{4\parallel}}(\alpha_1^4 + \alpha_2^4) \\ &= \mathrm{K_{2\perp}}\sin^2(\theta) - \frac{1}{2}\mathrm{K_{4\perp}}\cos^4(\theta) - \frac{1}{8}\mathrm{K_{4\parallel}}(3 + \cos(4\phi))\sin^4(\theta)\end{aligned} \tag{2.12}$$

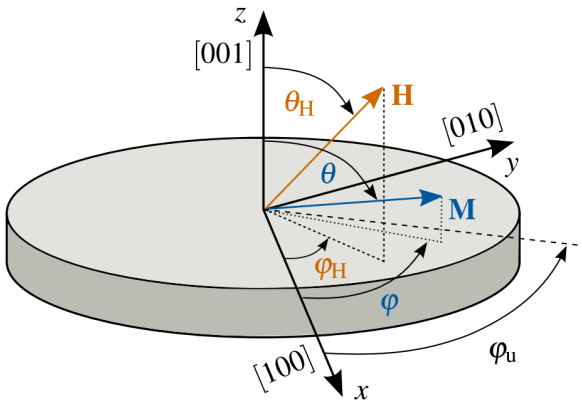

Fig. 2.1.: Sphercial coordinates, used to describe the free enthalpy. θ_H and ϕ_H are the angles corresponding to $\vec{H}$, while θ and ϕ represent the magnetsiation $\vec{M}$. The image was taken from [9].

Free enthalpy of the FeRh system

The total free enthalpy density of the studied FeRh system , G_{Ani}, is the total of every anisotropy, discussed above [9].

$$\begin{aligned} G_{Ani} &= F_{dd} + F_{Uni,\parallel} + F_{Uni,\perp} + F_{tet} - \vec{M} \cdot \vec{B}_{ext} \\ G_{Ani} &= -\vec{B} \cdot \vec{M} \left[\sin(\theta)\sin(\theta_B)\cos(\phi - \phi_B) + \cos(\theta)\cos(\theta_B)\right] \\ &\quad - K_{2\parallel} \sin^2(\theta)\cos^2(\phi - \phi_u) - \sin^2(\theta)\left(\frac{\mu_0 M^2}{2} - K_{2\perp}\right) \\ &\quad - \frac{1}{8}K_{4\parallel}\sin^4(\theta)(\cos(4\phi) + 3) - \frac{1}{2}K_{4\perp}\cos^4(\theta) \end{aligned} \tag{2.13}$$

The term $\mu_0 M_{eff}$ can be derived by

$$\mu_0 M_{eff} = \mu_0 M_S - \frac{2K_{2\perp}}{M_S}\,, \tag{2.14}$$

this is the effective magnetisation $\mu_0 M_{eff}$. It is formed by the difference between the shape anisotropy field and the perpendicular uniaxial anisotropy field. It decides whether the magnetisation prefers a direction parallel or perpendicular to the plane. If $\mu_0 M_{eff}$ is positive, the magnetisation prefers an orientation parallel to the sample surface, where as with a negative $\mu_0 M_{eff}$ the magnetisation prefers a direction perpendicular to the sample surface [9]. An illustration of how the system behaves by means of each anisotropy constant is visible in Ch.(A.2).

2.2. Magnetisation Dynamics

In the previous section 2.1 only the preferred direction, the easy axis, of the magnetisation was described. For that no external force was considered. Therefore, this direction is only valid for the equilibrium, where no external force will deflect the magnetisation. A rotation out of the equilibrium position is only possible in conjunction with an external force, since a potential landscape is created by various interactions Ch.(2.1), the deflection of $\vec{M}$ at a constant force is different for different directions.

A ferromagnet consist of many magnetic moments, μ_B, generated by the electrons of their atoms. Assuming a strong coupling to the nearest neighbour, a rotation of one moment, or spin, carries the rotation of all other spins, it therefore gives rise to the macroscopic magnetisation $\vec{\mathrm{M}}$ for homogeneous magnetised samples, where the magnetisation $\vec{\mathrm{M}}$ is written as the vectorial sum of all spins $\vec{\mathrm{M}} = \mu_{\mathrm{B}}\mathrm{V}$, where V is the volume of the sample [6]. The direction of $\vec{\mathrm{M}}$ in the equilibrium is parallel to an effective magnetic field $\vec{\mathrm{B}}_{\mathrm{eff}}$. It takes every field which is affecting $\vec{\mathrm{M}}$ into account, such as a externally applied field $\vec{\mathrm{B}}_{\mathrm{ext}}$, the field that can be derived by the anisotropic contributions $\vec{\mathrm{B}}_{\mathrm{ani}} = -\frac{1}{M}\nabla_m \mathrm{G}_{\mathrm{Ani}}$ and an exchange field $\vec{\mathrm{B}}_{\mathrm{exch}}$ of the interaction with the nearest neighbour [3].

$$\vec{\mathrm{B}}_{\mathrm{eff}} = \vec{\mathrm{B}}_{\mathrm{ext}} + \vec{\mathrm{B}}_{\mathrm{ani}} + \vec{\mathrm{B}}_{\mathrm{A}} \tag{2.15}$$

If $\vec{\mathrm{M}}$ gets deflected out of the easy axis, a torque $\vec{\mathrm{T}}$ emerges.

$$\vec{\mathrm{T}} = \vec{\mathrm{M}} \times \vec{\mathrm{B}}_{\mathrm{eff}} \tag{2.16}$$

Ideally, $\vec{\mathrm{B}}_{\mathrm{eff}}$ should be perpendicular to $\vec{\mathrm{M}}$ to avoid further contributions and therefore a more difficult calculation. The torque forces the magnetisation $\vec{\mathrm{M}}$ to precess around its equilibrium position. In the process $\vec{\mathrm{M}}$ has an orbital momentum $\vec{\mathrm{L}}$, which is related to the magnetic moment μ_B, by $\mu_B = V\vec{\mathrm{M}}$ [10].

$$\vec{\mathrm{L}} = -\frac{\mu_B}{\gamma} = -\frac{V}{\gamma}M \tag{2.17}$$

With the commonly used equation of motion $\frac{\mathrm{dL}}{\mathrm{dt}} = T$, one obtains the Landau Lifshitz Equation (LL-Equation) [3, 10].

$$\frac{\mathrm{d}\vec{\mathrm{M}}}{\mathrm{dt}} = -\gamma\vec{\mathrm{M}} \times \vec{\mathrm{B}}_{\mathrm{eff}} + \lambda\vec{\mathrm{M}} \times (\vec{\mathrm{M}} \times \vec{\mathrm{B}}_{\mathrm{eff}}) \tag{2.18}$$

Equation (2.18) describes the motion of $\vec{\mathrm{M}}$ inside an external field with respect to the magnetic anisotropy and damping. It already has an additional phenomenological damping term added. This damping has to be a part of this equation, in order to ensure physical correctness, without it the magnetisation would never stop precessing around the easy axis. The damping can be explained as an additional force which tries to counteract the precession. Therefore the term $\mathrm{F}_\lambda = \lambda\vec{\mathrm{M}} \times (\vec{\mathrm{M}} \times \vec{\mathrm{B}}_{\mathrm{eff}})$ can be added.
In 1955, Gilbert discovered that the LL-Equation behaves non-physically for large damping parameters λ. He then formulated the Gilbert equation named after him, which completes the LL-equation to the Landau-Lifshitz-Gilbert-Equation (LLG) [11].

$$\frac{\mathrm{d}\vec{\mathrm{M}}}{\mathrm{dt}} = -\frac{\gamma}{1+\alpha^2\mathrm{M}^2}\vec{\mathrm{M}} \times \vec{\mathrm{B}}_{\mathrm{eff}} + \frac{\alpha\gamma}{1+\alpha^2\mathrm{M}^2}\vec{\mathrm{M}} \times (\vec{\mathrm{M}} \times \vec{\mathrm{B}}_{\mathrm{eff}}) \tag{2.19}$$

Here γ is the gyromagnetic ratio, $\gamma = \frac{\mathrm{g}\mu_{\mathrm{B}}}{\hbar}$, where g is the Landé factor. In addition to λ Gilbert introduced a new damping parameter, α.

2.3. Ferromagnetic Resonance / FMR

Ferromagnetic resonance describes the phenomenon that a ferromagnet absorbs electromagnetic radiation, when exposed to an external magnetic field. A first successful ferromagnetic resonance experiment was conducted by Griffith on various metallic thin films in 1946 [12].
As already described in Eq.2.2, an external field brings the magnetisation to precession. The

greater the field strength, the greater the angle of the precession cone. The precession frequency can be approximately described by the Larmor frequency [6, 10].

$$\omega_{\text{res}} = \gamma \vec{\text{B}}_{\text{eff}} \tag{2.20}$$

If the sample is irradiated with microwaves, resonant absorption occurs when the circularly polarised part of the electromagnetic wave oscillates at the same frequency as the precession of the magnetisation. As previously stated, the anisotropy creates a potential landscape. In this landscape an oscillator can be described by means of a small angle approximation to the equilibrium position. This shows the proportionality of the resonance frequency with its system's Hessian matrix [13].

$$\omega_{\text{res}} = \pm \frac{\gamma}{\text{M}\sin(\theta_M)} \sqrt{\frac{\partial^2 \text{G}_{\text{Ani}}}{\partial \theta_{\text{M}}^2} \frac{\partial^2 \text{G}_{\text{Ani}}}{\partial \phi_{\text{M}}^2} - \frac{\partial^2 \text{G}_{\text{Ani}}}{\partial \theta_{\text{M}} \partial \phi_{\text{M}}}} \tag{2.21}$$

3. Methods

3.1. Measurement Setup

All FMR measurements were perfomed using a Bruker brand Elexsys-II-500 system. The experimental system consists of a water-cooled magnet, which can produce up to 1.6 T or 2.1 T depending on the configuration, as described in section 3.1.3. In addition, a spectrometer is used, which includes a lock-in amplifier and a server to control the spectrometer from a Linux computer. A schematic illustration of the system is given in Fig. 3.1.

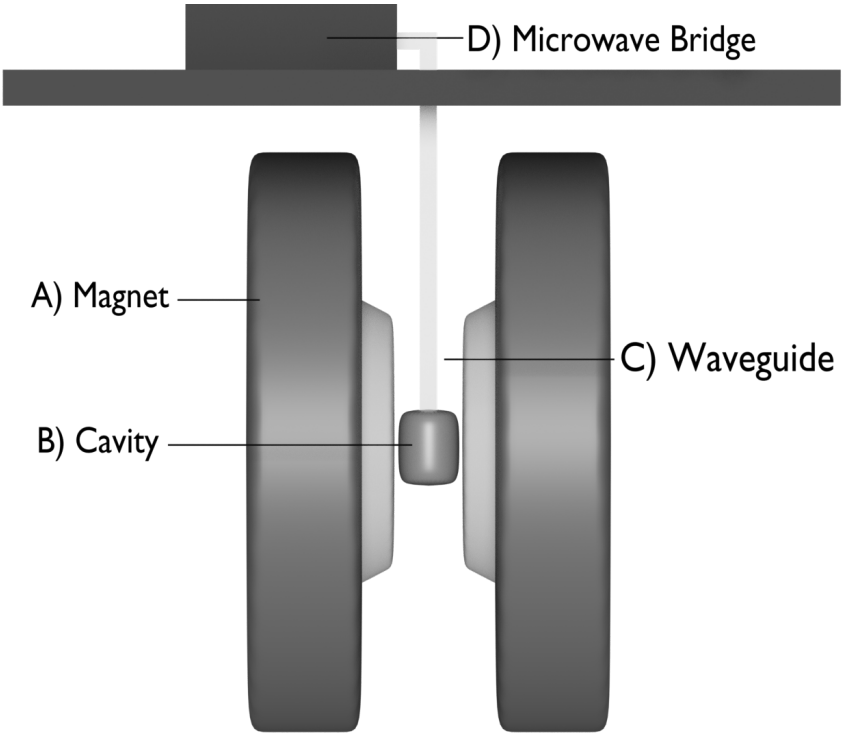

Fig. 3.1.: Schematic illustration of EPR system (Elexsys-II-E500). A cylindrical cavity is mounted without additional pole pieces

3.1.1. Electron Paramagnetic Resonance / FMR Spectrometer

The experimental system used in this thesis was developed for Electron Paramagnetic Resonance (EPR). The external magnetic field causes a Zeeman splitting of the energy levels of a paramagnet. If the sample is irradiated with microwaves, they cause a spin flip of electrons when absorbed. This absorption is detected by the lock-in amplifier. This system is best suited for the ferromagnetic resonance. Although no Zeeman splitting is produced with ferromagnets, the microwaves are absorbed by the precession caused by the external field, which in turn can

be measured analogously to the Electron Paramagnetic Resonance.
The experimental system used in this thesis consists of a microwave bridge, a microwave conductor and a cavity resonator. To measure the ferromagnetic resonance, there are 2 approaches. In the first approach, one uses a constant external magnetic field and does a sweep over a range of microwave frequencies. In the second approach one keeps a microwave frequency constant and varies the external magnetic field. In this work the latter method was used. This offers a much higher sensitivity, since a resonator can be used. Due to the cavity to amplify only certain wavelengths, this prevents the changing of the wavelength. As a result, only the field is varied until the so-called resonance field has been detected, this field is frequency-dependent. The resonator eliminates the variability of the frequency. The used resonators work in the so-called X-Band. This offers a frequency range of 8-12 GHz. The microwave bridge operates in the same frequency band. This serves as a microwave source and detector at the same time.

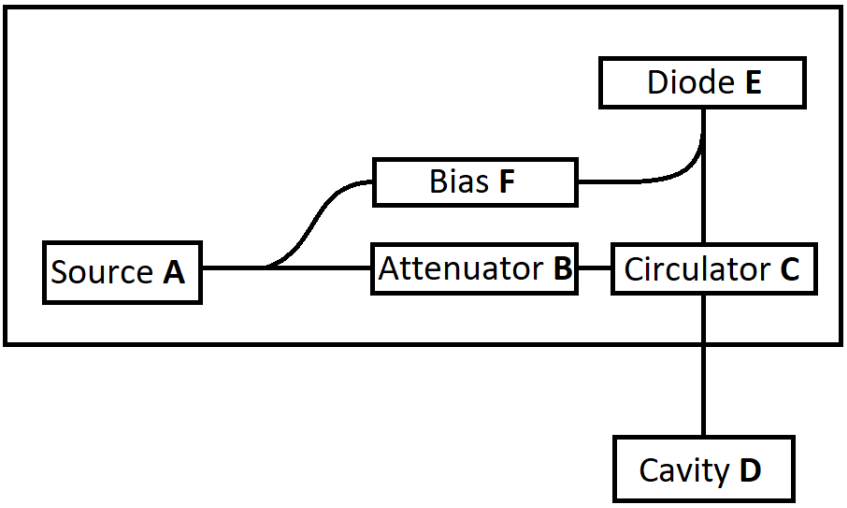

Fig. 3.2.: Schematic illustration of the microwave bridge

Fig. (3.2) shows the schematic illustration of the microwave bridge. Here **A** is the microwave source, from there the waves go to an attenuator **B**. With this, one can adjust the microwave power precisely. The damped radiation then reaches the sample in resonator **D**, where it is absorbed. Absorption results in the breakage of the impedance matching of the resonator and the microwave conductor. As a result, microwaves are now reflected from the resonator back to the microwave bridge. Component **C** now ensures that only the reflected radiation is transmitted to the detector **E**. The detector **E** consists of a diode, which converts the microwave power into a current. The diode achieves the best results in a current range around 200 μA. There, the diode current is proportional to the square root of the microwave power. To ensure that the diode works in the optimum range of 200 μA, the so-called reference arm **F** is present. It shunts part of the radiation from the source, attenuates it and shifts its phase, so that the so-called bias has the same phase as the reflected radiation [14].

3.1.2. FMR and EPR signal line shape

In order to measure an absorption signal, the phase-sensitive detection of a lock-in amplifier is used. In addition to the external magnetic field, the cavity uses so-called modulation coils to generate a magnetic field whose intensity oscillates sinusoidally with an applied modulation frequency. The cavities used in this work are designed for frequencies of 100 kHz. If an absorption

appears, the microwaves get reflected from the cavity to the lock-in amplifier. Meanwhile, the magnetic field strength in the cavity is changed according to the modulation frequency. Thus, the reflected waves have a mutually distinguishable modulated amplitude, depending on the time of their reflection. The receiver now assumes,that on an interval as wide as the modulated amplitude is large, the signal behaves linearly. The signal can therefore be transformed into a sine wave whose amplitude is proportional to the slope of the signal. Thus, the first differential of the signal becomes measurable [14].
A suitable description of resonance problems offers the Cauchy distribution, often called Lorentz distribution. It describes the distribution of the y-intercept b of a line at random angle to the y-axis intersecting the x-axis [15].

$$\begin{aligned} \mathrm{P} &= \frac{\mathrm{A}}{\pi \mathrm{R}\left(\frac{(\mathrm{B}-\Delta\mathrm{B})^2}{\mathrm{R}^2}+1\right)} \\ \frac{\mathrm{dP}}{\mathrm{dB}} &= -\frac{\mathrm{A}(2(\mathrm{B}-\Delta\mathrm{B}))}{\pi \mathrm{R}^3\left(\frac{(\mathrm{B}-\Delta\mathrm{B})^2}{\mathrm{R}^2}+1\right)^2} \end{aligned} \tag{3.1}$$

A is the Amplitude, ΔB is the Linewidth, R is the resonance field and B is the external magnetic field. Using the first derivative of the Cauchy distribution one can fit an ideal EPR or FMR signal. In reality, however, other effects must be considered. Effects such as diffusion time of charge carriers of the sample, skin depth and relaxation times, respectively effects of conductive thin films, lead to an unequal distribution of the microwave fields in the sample. This inequality causes an asymmetry of the line shape. In such samples the line is therefore shifted up or down around its midpoint [16].
Dyson dealt with this problem in 1955 and modified the Cauchy distribution with an additional asymmetry parameter $0 \leq \alpha \leq 1$.

$$\begin{aligned} \mathrm{D} &= \frac{4\mathrm{A}\Delta\mathrm{B}^2\left(\alpha(\mathrm{B}-\mathrm{R})+\sqrt{3}\Delta\mathrm{B}\right)}{\sqrt{3}\left(4(\mathrm{B}-\mathrm{R})^2+3\Delta\mathrm{B}^2\right)} \\ \frac{\mathrm{dD}}{\mathrm{dB}} &= \frac{4\mathrm{A}\Delta\mathrm{B}^2\left(3\alpha\Delta\mathrm{B}^2-4\alpha(\mathrm{B}-\mathrm{R})^2-8\sqrt{3}\Delta\mathrm{B}(\mathrm{B}-\mathrm{R})\right)}{\sqrt{3}\left(4(\mathrm{B}-\mathrm{R})^2+3\Delta\mathrm{B}^2\right)^2} \end{aligned} \tag{3.2}$$

Due to strong asymmetry the Dyson function is used in the further course of this work. The distorted FeRh gains additional asymmetry through competing antiferromagnetic and ferromagnetic phases [17].

3.1.3. Angular dependence setup for FMR measurements

As described in Eq.(2.21), the resonance frequency or the resonance field is angular dependent. Changing the angle of the sample relative to the external field allows to determine the magnetic anisotropy of the sample. To rotate the sample inside the resonator a goniometer is used. It is connected to a computer which controls a motor to rotate the sample to a certain angle. In the course of this work, different setups were used to measure the temperature dependence or measure at stronger fields in addition to the room temperature angle dependence.

Temperature dependent FMR

Temperature dependent Measurements were carried out in a temperature range from 100 K to 450 K. For low temperature measurements, a glass cryostat is installed inside the resonator. Additionally the cryostat has a heating coil attached to the bottom. Using the cryostat, liquid nitrogen can be heated to fill the resonator with cold nitrogen gas. Using this method, a temperature of 100 K can be achieved. The temperature is continuously monitored by a temperature sensor. Subsequently, a temperature controller controls the flow of liquid nitrogen. In addition, the heating coil power can be controlled, in order to regulate and stabilise temperatures.
In principle, the construction for low temperatures can also be used to do measurements for high temperatures, by employing a nitrogen gas of room temperature which is then heated to desired temperature range.

High Field Setup for FMR

In the case of this Bruker system the maximum field strength is 1.6 T. Here the power supply of the magnet is reaching the limit of 150 A. By attaching pole shoes to the magnets, the maximum field increases to 2.1 T, by reducing air gap between the pole shoes of the electromagnet. The disadvantage of this construction is that the space for the resonator is reduced. The type used here is a rectangular Varian resonator, with a smaller cross section than the previously used cylindrical Bruker resonator. Cylindrical resonators have a higher quality factor Q than rectangular ones and thus are more sensitive.

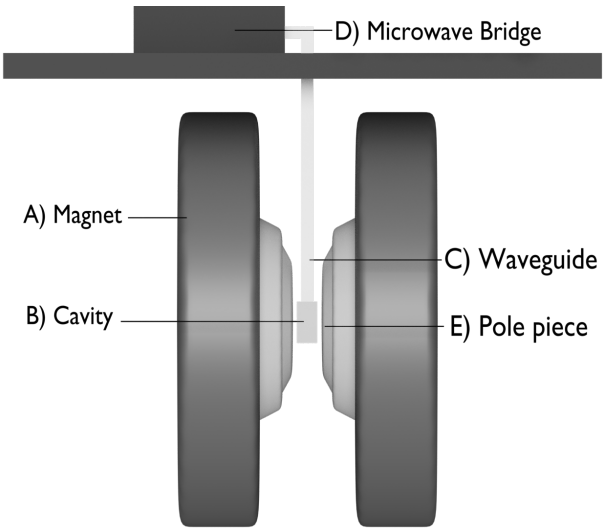

Fig. 3.3.: Elexsys-II-E500 Schematic with pole pieces **E**. The place for the cavity got narrower, therefore the rectangular Varian cavity, which is smaller in diameter, needs to be mounted

3.2. FeRh thin films

The samples used in the work are FeRh thin films with a thickness of 40 nm. The FeRh alloy is grown on MgO [001] substrates. All samples have a composition of about 50% iron and 50% rhodium. They were irradiated with different fluences from $1 \cdot 10^{13}$ Ions / cm^2 up to $4 \cdot 10^{13}$ Ions / cm^2 of low energy Neon ions.

3.2.1. Preparation of FeRh thin films

Magnetron Sputtering

Magnetron sputtering was used to deposit the FeRh layers to the MgO substrate. Magnetron sputtering is an advanced system of the basic sputtering process. During the sputtering process, a cathode consisting of the material, in this case an FeRh alloy, is bombarded with a high energy Argon ions. The ions form in a plasma which is localised in front of the cathode. The bombardment with Ar ions separates atoms from the target. The sputtered atoms then condense on the MgO (001) substrate and form a thin film. In addition, as a by-product of the process, so-called secondary electrons are formed on the target, which contribute to the stability of the plasma.
This is where magnetron sputtering comes in effect. A magnetic field is now created parallel to the target surface. This field limits the movement of the secondary electrons by the induced Lorentz force. This increases the probability of electron collisions in the plasma and thereby the ionisation rate. The ionisation rate, in turn, is decisive for the sputtering process. This results in higher deposition rates on the substrate during magnetron sputtering than in conventional sputtering.
In the case of the FeRh thin films, the target consisted of an alloy made of 50/50 FeRh as a bulk. The target then was brought to a temperature of 600°C for sputtering. After the magnetron sputtering, each sample was heated to 750°C to achieve the B2 structure. This post annealing process was performed for 1 to 2 hours. Utilising Rutherford Back-Scattering, an atomic distribution of 50.4% iron and 49.4% rhodium was measured, the results are shown in Fig.(3.4) [18].

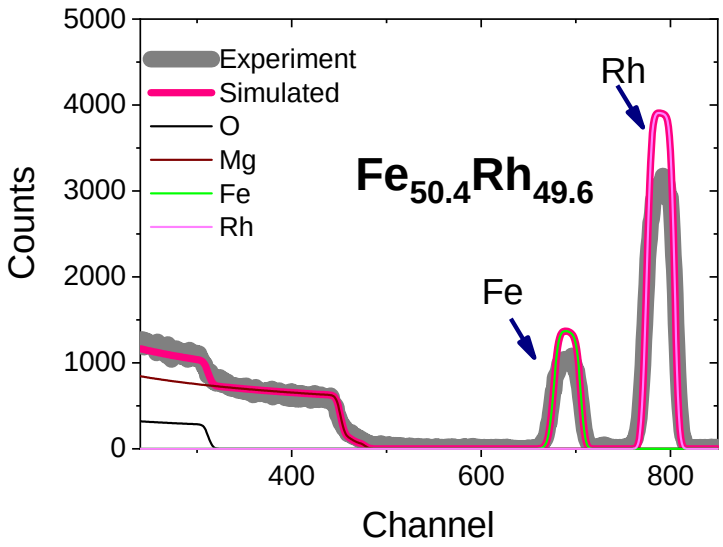

Fig. 3.4.: Rutherford Back-Scattering of the FeRh samples after the magnetron sputtering [19]

Neon-Ion Irradiation

The thin FeRh films produced by the magnetron sputtering are in an ordered crystal structure especially after the post annealing process. In order to create a disorder, the FeRh thin films were irradiated with Neon ions, which had an energy of 25 keV. For this purpose, a broad ion beam was generated, which homogeneously covered the samples. Cervera et al. used this method of irradiation on FeRh thin films with a thickness of 35 nm [20]. The energy of the Neon ions

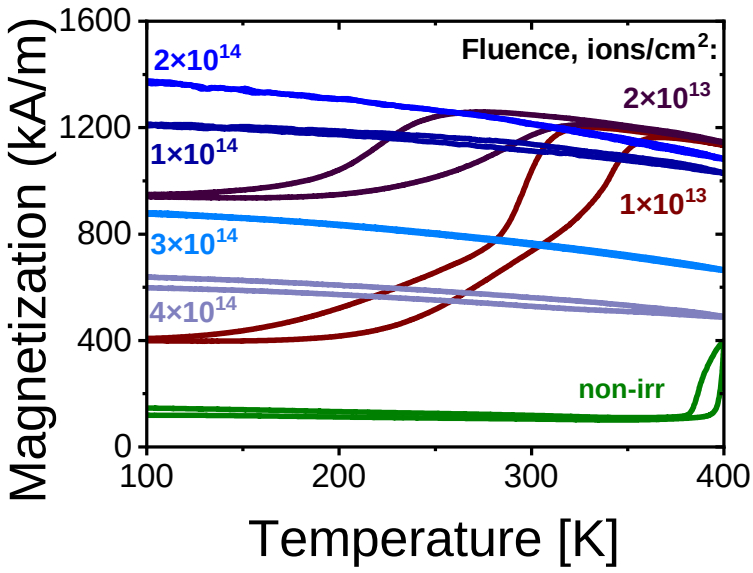

Fig. 3.5.: Temperature dependence of magnetisation of FeRh irradiated with different fluence [19]

is chosen so that the atomic elastic collision is the dominant process in the interaction with the FeRh atoms. The difference to the samples investigated in this work is the angle and the intensity of the irradiation. Cervera et al. used an angle of 60° between thin film normal and ion beam. This is used to prevent channelling of the ions. Here, the ions can pass through the samples without interchanging with the FeRh atoms. The samples used in this work therefore were irradiated with an angle of 7° in respect to the film surface.
The intensity of the irradiation is described with the fluence Φ. It is composed of the quotient of the number of particles N and the target area A. The samples have a fluence of $1 \cdot 10^{13} \frac{\text{Ions}}{\text{cm}^2}$ up to $4 \cdot 10^{14} \frac{\text{Ions}}{\text{cm}^2}$. Fig.(3.5) shows the magnetisation for different temperatures depending on the fluence. For comparison, a reference sample without irradiation is shown. This shows the typical 2 magnetic phases of FeRh [21], depending on the existing phase the magnetisation changes, which is why a temperature hysteresis curve is formed. As the fluence increases, so does the magnetisation. The samples with the fluence of $10^{13} \frac{\text{Ions}}{\text{cm}^2}$ show of 2 phases. The remaining samples of the order of $10^{14} \frac{\text{Ions}}{\text{cm}^2}$ only have one phase. This tuneable phase transition has already been observed by Heidarian (2015) on similar irradiated samples produced with molecular beam epitaxy [22]. Note that ion bombardment is not confined to Neon alone, so similar results were obtained with bombardment of highly energetic ions in the MeV range [23, 24]. However, in order to not damage the crystal lattice with high energy ions, lighter elements such as helium or hydrogen were used.

3.2.2. Properties of FeRh thin films

The FeRh thin films are an alloy of about 50% Fe and 50% Rh. In the ordered and non-irradiated state, layers of Fe and Rh atoms form a B2 (CsCl) structure, shown in Fig.(3.6). A unit cell consists of a rhodium atom in the middle surrounded by 4 iron atoms located in the corners of the cell. The peculiarity of FeRh resides in the presence of 3 different phases, antiferromagnetic (AF), ferromagnetic (FM) and paramagnetic, first observed by Fallot and Hacort (1939) [25]. The FeRh alloy undergoes a first-order phase transition from AF to FM phase at a temperature of 370K. Further investigations by Lommel show a correlation of the phase transition temperature of the transition with the concentration of Rh atoms [26]. Lommel's FeRh bulk samples had 51%

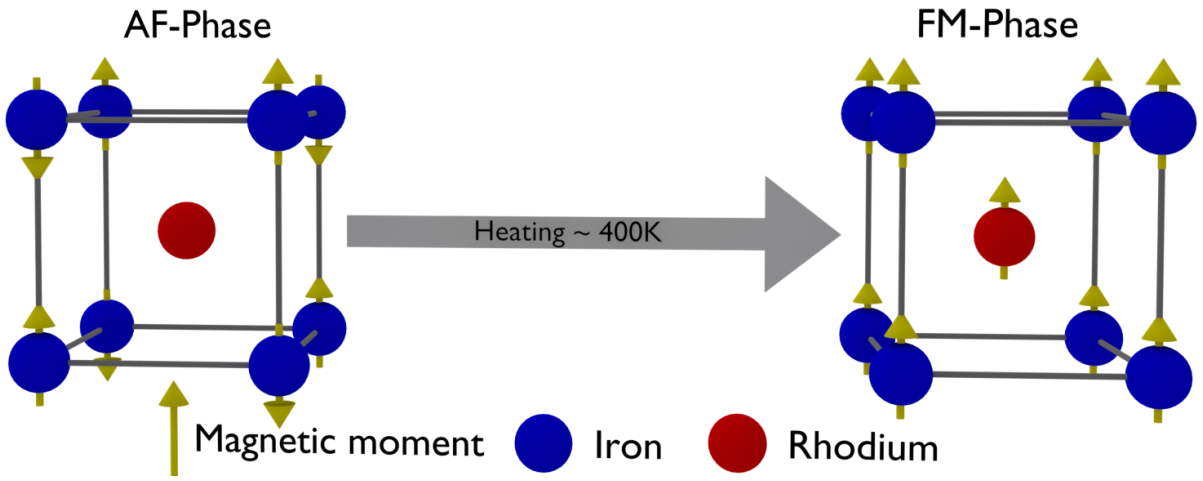

Fig. 3.6.: Thermally induced phase transition from the antiferromagnetic phase to the ferromagnetic phase. In the AF-Phase the rhodium atoms have no magnetic moment, whilst they contribute to the magnetisation in the FM-phase

Rh content, which is enough to shift the phase transition temperature to 330K. In addition, he observed a Curie temperature of 700K in the FM phase. The phase transition is also manifested by an increase in volume [27], changes in electrical resistance [28] and specific heat [29]. The contribution of the individual atoms to the magnetisation depends on the respective phase, so that the Fe atoms have a magnetic moment of $3.3\mu_B$ in the AF state, the Rh atoms do not contribute. Above the phase transition, the Rh atoms have a magnetic moment of $0.9\mu_B$ and the Fe atoms have a moment of $3.2\mu_B$ [30]. In addition the thin films show a hysteresis in the M-T diagram Fig.(3.5), which is indicative of the presence of both FM and AF phase [31].
Mancini et al. have already investigated the FMR linewidth ΔH and anisotropy of an ordered 50 nm FeRh thin film in FM phase [30]. The results are shown in Table (3.1). Mancini also describes the nucleation of FM domains in the AF phase, when the phase transition temperature T_C is exceeded, the nucleation process begins, it is illustrated in Fig.(3.7). Furthermore, a M-T hysteresis curve can be seen, since the phase transition temperatures of the respective phases are different, i.e. T_{AF} the phase transition Temperature from AF to FM state is smaller than T_{FM} from FM to AF. Mancini explains this by a net magnetic moment which stabilises the FM phase and thus generates a magnetic inertia [30]. The same effect has also been described by Cervera with respect to irradiated thin films [20].

Table 3.1.: Anisotropy constants for an ordered FeRh thin film with 50 nm thickness,according to Mancini et al. [30]

Constant	$K_{2\perp}$	$K_{2\parallel}$	$K_{4\perp}$	$K_{4\parallel}$
Value [J / m^3]	$(5.2 \pm 0.1) \times 10^5$	$(7.3 \pm 1.6) \times 10^2$	(2.3 ± 8)	$(6.4 \pm 0.8) \times 10^3$

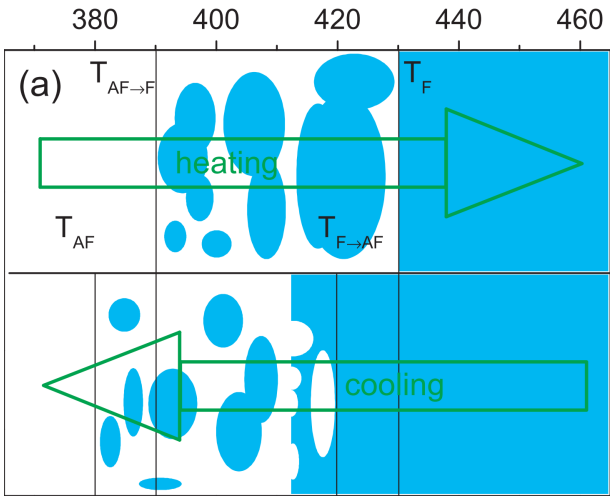

Fig. 3.7.: Nucleation of ferromagnetic or antiferromagnetic domains in FeRh while heating or cooling. The phase transition temperature differs depending if one is cooling or heating the thin film. The nucleation of domains of the corresponding phases begins after exceeding the current phase transition temperature. The figure was taken from Mancini et al. [30]

4. Results and discussion

The following chapter presents the results of the FMR experiments on irradiated FeRh thin films. The thin films were sorted and named according to the used fluence, i.e. the thin film with the lowest fluence, here $1 \cdot 10^{13}$ ions / cm^2, is called FeRh-1. In Table (4.1) the fluences and the corresponding names are given.
The in-plane (azimuthal, ϕ) and the out-of-plane (polar, θ) angular dependences of the magnetisation of FeRh thin films have been measured. In-plane means that the external magnetic field is applied parallel to the surface of the thin film, the polar angle θ has a value of $\theta = \pi/2 = 90°$, the azimuthal angle ϕ is then changed by 360 ° in certain angular steps. During the measurements, the MgO [001] is exactly perpendicular to the external magnetic field. Due to the manual positioning of the sample, the start values of ϕ can slightly vary around the in-plane hard axis of FeRh.
In the evaluation of the out-of-plane measurements, an azimuthal angle $\phi = \pi$ / 4 was assumed. The FeRh grows at 45° offset to the [001] axis of the MgO. Hence the thin films were fixed in a direction that MgO [001] is perpendicular to the magnetic field, a correction for the axes of the FeRh thin film results in an offset by $\phi \approx 45°$.
Temperature plays a major role in the measurement of FeRh thin films, because the transition temperature changes depending on the fluence present. Thus, FeRh-1 and FeRh-2 can have two phases between 100 K and 400 K, see Fig. (3.5). To study the effect of temperature on anisotropy in the FeRh films, measurements were made between 100 K and 450 K. Due to the limited time of the bachelor thesis not all thin films could be examined. All temperature measurements were carried out in in-plane direction.

4.1. Measurements of FeRh thin films with low fluence

4.1.1. FeRh-1

FeRh-1 in-plane measurement

The FMR spectrum of FeRh-1 was measured at room temperature. The microwaves had a frequency of 9.4567 ± 10^{-5} GHz and a power of 20 mw. The angular dependence was performed for 360° in 3° steps, the external magnetic field was varied from 0 T to 0.8 T. The measurement is

Table 4.1.: FeRh thin films sorted by the used fluence, the corresponding saturation magnetisation M_S and overall area, beginning with the unirradiated and ending at the most irradiated thin film. Everything was measured at room temperature.

Thin film	FeRh-0	FeRh-1	FeRh-2	FeRh-3	FeRh-4	FeRh-5	FeRh-6
Fluence [ions / cm^2]	0	$1{\cdot}10^{13}$	$2{\cdot}10^{13}$	$1{\cdot}10^{14}$	$2{\cdot}10^{14}$	$3{\cdot}10^{14}$	$4{\cdot}10^{14}$
Magnetisation M_S [A / M]	$0.285{\cdot}10^6$	$1.04{\cdot}10^6$	$1.27{\cdot}10^6$	$1.213{\cdot}10^6$	$1.282{\cdot}10^6$	$0.809{\cdot}10^6$	$0.644{\cdot}10^6$
Size [mm^2]	12.5	3.75	1.5	2.5	5	5.25	5

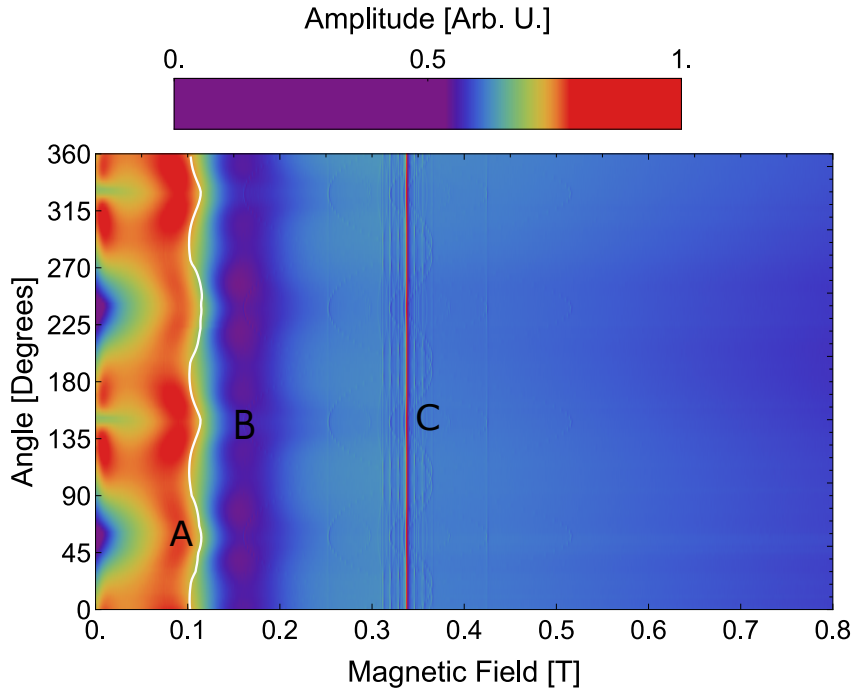

Fig. 4.1.: In-plane angular dependent FMR of FeRh-1 displayed in a colour plot; measured at f = 9.4567 ± 10^{-5} GHz and microwave power of 20 mW

shown in a colour diagram in Fig. (4.1). In the colour diagram, a colour was assigned to a corresponding amplitude value. The main signal **A** of FeRh can be seen in the magnetic field range of 0 - 0.2 T. The white line around 0.1 T is the fitted resonance position of the main signal superimposed with the colour diagram. The resonance position has a maximum at $(0.1153 \pm 1 \cdot 10^{-4})$ T at an angle $249° \pm 3°$, the minimum resonance field is $(0.1014 \pm 1 \cdot 10^{-4})$ T at $288° \pm 3°$. The maximum resonance field characterises the hard axis, the main signal **A** shows a repetition of the maxima in total every 90°, one speaks therefore of a fourfold symmetry. The same applies to the easy axis, visible here as the minima of the resonance field. The observed fourfold symmetry is related to the cubic crystal lattice of FeRh. Based on the small difference between absolute minimum and absolute maximum, the cubic anisotropy is small, that the corresponding anisotropy constant $K_{4\parallel}$ will also be small. In addition, the uniaxial anisotropy $K_{2\parallel}$ is given by the difference between the maxima, with regards to FeRh-1-in-plane $K_{2\parallel}$ will be small.

The extrema of the resonance field also differ and have about the same value every 180°. This can be explained in addition to the fourfold symmetry by assigning another twofold symmetry. The twofold symmetry rises from the uniaxial anisotropy, which is present in only two directions. Noticeable is the greater width of the hard axis in the range 45° - 90° and 270° - 225°, these extrema are here named 1^{st} order, compared with 135° - 180° and 315° - 360°, here 2^{nd} order. In addition, there is an weak 8-fold symmetry **B** in a magnetic field range around 0.14 T. The last two visible effects could be the cause of an overlapping or coupling of the main line **A** with another smaller line. This second line has a much stronger hard axis, which must lie in the areas of the 2^{nd} order, since the local maxima appear undistorted and the signals can not be superimposed.

A superposition of the two signals can be seen in the 1^{st} order, since the broad maximum has 2 additional subordinate maxima. This second line has a twofold symmetry and therefore must be a uniaxial contribution with minima in the ranges (45° - 90°)$\pm$ 3° and (225° - 270°)$\pm$ 3 °, further effects with an external magnetic field of 0 T are excluded, since FeRh-1 has a coercive

field of 88 Oe. This means that the 1^{st} order maxima are in the area in which the hard axis of the second line forms, thus the two signals overlap and the subordinate maxima arise. Therefore, the additional twofold symmetry that produces the 1^{st} and 2^{nd} order maxima is an effect of superposition of the main line with a weaker secondary line.
For field strengths in the range of 0.15 T - 0.5 T, further angle-dependent signals and angle-independent signals can be identified **C**. The angle-independent signals do not form from the FMR, they are an EPR signal originating from the substrate. The angle-dependent components are the signals of the associated crystal field of the MgO.
The origin of the secondary line can not be completely determined at present. One hypothesis would be that the irradiation of the Ne^+ ions at a certain angle has brought additional symmetry caused by collision into the crystal structure.

FeRh-1 out-of-plane measurement

The measurement was carried out for a microwave frequency of 9.8230 ± 10^{-5} GHz at 2 mW. The external magnetic field was varied from 0 T to 0.2 T. The angle dependence was determined for 360° in 1° steps. In the colour diagram Fig. (4.2a) a uniaxial anisotropy **A** is observed. At about 90° and 270° sample has a hard axis **B** which extends beyond the considered magnetic field. The main signal also shows a vertical line **C** when the hard axis is reached, the amplitude decreases and finally vanishes up to a magnetic field of 1.2 T. The easy axis is at values of $(0.1429 \pm 1 \cdot 10^{-4})$ T at 175° ±0.5° and $(0.143 \pm 1 \cdot 10^{-4})$ T at 354° ±1°. In addition to the uniaxial main signal **A** another signal **D** can be seen. This is in the range (0.3-0.4) T and shows no angular dependence. Signal **D** is the signal of the impurities of the used substrate MgO. These signals can be paramagnetic, or in the worst case ferromagnetic. An EPR signal does not show any angular dependence and is therefore visible as a vertical line in the colour diagram. To determine the resonance position of the hard axis, the thin film was measured in the high field setup (HF-setup). This measurement is shown in Fig (4.2b). The microwaves had a frequency of 9.5047 ± 10^{-5} GHz with a power of 20 mW, measured from 1.2 T to 2.1 T in an angle of 82° to 100° in 0.5° increments. The hard axis thus has a resonance position of $(1.572 \pm 1 \cdot 10^{-4})$ T at an angle of 89° ±1°. Here, the angle of the HF measurement was adapted to the signal **A**. The signal **E** was fitted. The resonance position is recognisable as a white curve. A line pointed with **F** shows a angular dependence, but because of the general shape it is more likely just a noise, like signal **G**.

Temperature dependent in-plane FMR measurements of FeRh-1 thin films

The thin film FeRh-1 was measured for temperatures of 100 K and 200 K, they are shown in Fig.(4.3). The frequencies were in the range of $9.42 \pm 1 \cdot 10^{-3} \pm 10^{-3}$ GHz, both had a microwave power of 20 mW. The temperature changes were ±0.2 K for 100 K and ±0.5 K for 200 K. An angular dependence was measured for 360° in 5° increments. Only the range of the external magnetic field varied. FeRh-1-100 K had a sweep width from 0 T to 1.2 T, while 200 K had only sweep width from 0 T to 0.5 T.
The main signal **A** of both measurements shows a cubic anisotropy superimposed with a uniaxial anisotropy. The maxima are in both measurements (60°, 150°, 235°, 325°) ± 5°, the resonance positions have values of $(0.222 \pm 1 \cdot 10^{-3})$ T and $(0.212 \pm 1 \cdot 10^{-3})$ T for 100 K. An additional uniaxial anisotropy shows itself through the different minima **B**, which have a 180° symmetry. Even the minima do not differ from each other in their angle values, so they are (10°, 105°, 195°, 280°) ± 5°. The 100 K measurement has the resonance positions (0.181 T, 0.181 T, 0.18 1T,

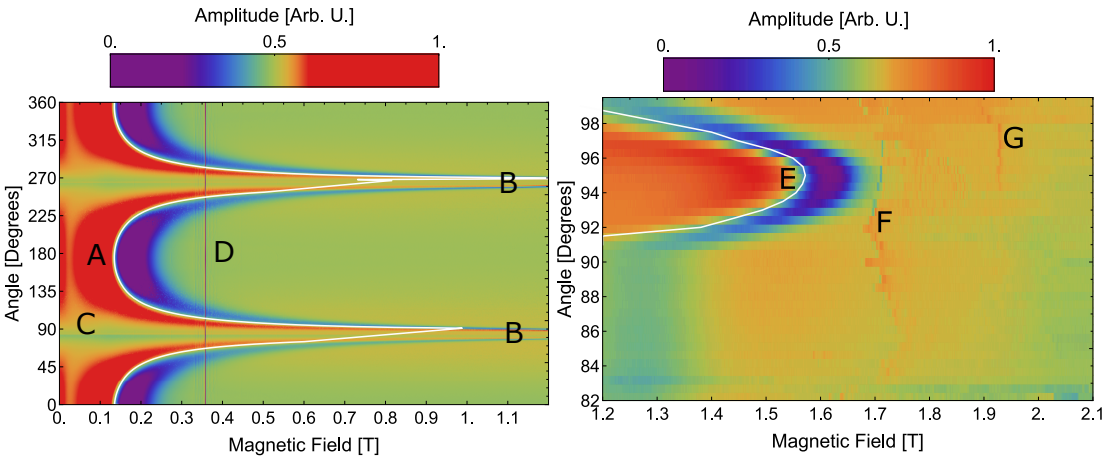

(a) FeRh-1 out-of-plane **(b)** FeRh-1 out-of-plane measured in high field

Fig. 4.2.: The high field measurement was done, in order to catch the hard axis. For this the setup was changed, to reach a magnetic field of 2.1 T

0.182 T) $\pm 1 \cdot 10^{-3}$T, while 200 K with (0.172 T, 0.174 T, 0.173 T, 0.174 T) $\pm 1 \cdot 10^{-3}$ T has a small variation in the minima. This variation is much more apparent in the colour diagram at point **C**. Signal **C** could represent the easy axis of an uniaxial signal, this would be in the range 90°-135° and gave a resonance position of 0 T - 0.15 T. It is visible in both temperature measurements, but has a larger amplitude at 200 K than at 100 K.
In addition, one can see a bright stripe **D** at an angle of about 190° and 15°, this is not a measurement error, as this is available in 100 K as well as in the 200 K measurement. This lighter stripe causes a splitting of the minima in **E**.
Compared to FeRh-1 in-plane measurement, the secondary signal becomes more visible at lower temperatures. As already assumed the secondary signal causes a variation of the minima, by overlapping of two minima of the cubic with easy axis of the uniaxial anisotropy **C**. This secondary signal creates stripes **D** in the hard axis, these remind of the horizontal lines of uniaxial anisotropy of out-of-plane measurements.

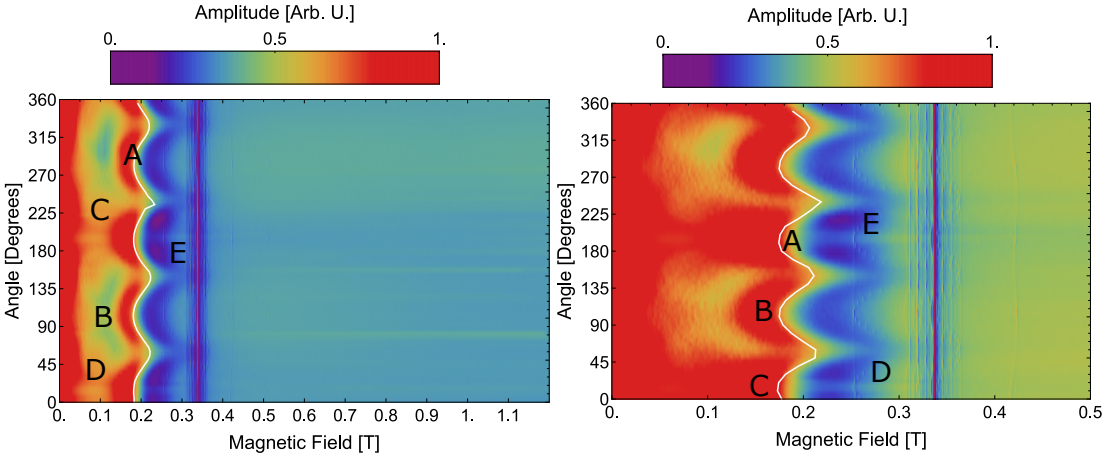

(a) FeRh-1 measured at a temperature of 100 K **(b)** FeRh-1 measured at a temperature of 200 K

Fig. 4.3.: The measurements for 100 K and 200 K were done in one session, that is why their angles are corresponding to the same axes. The white line is the fit for the resonance positions

4.1.2. FeRh-2

FeRh-2-in-plane measurement

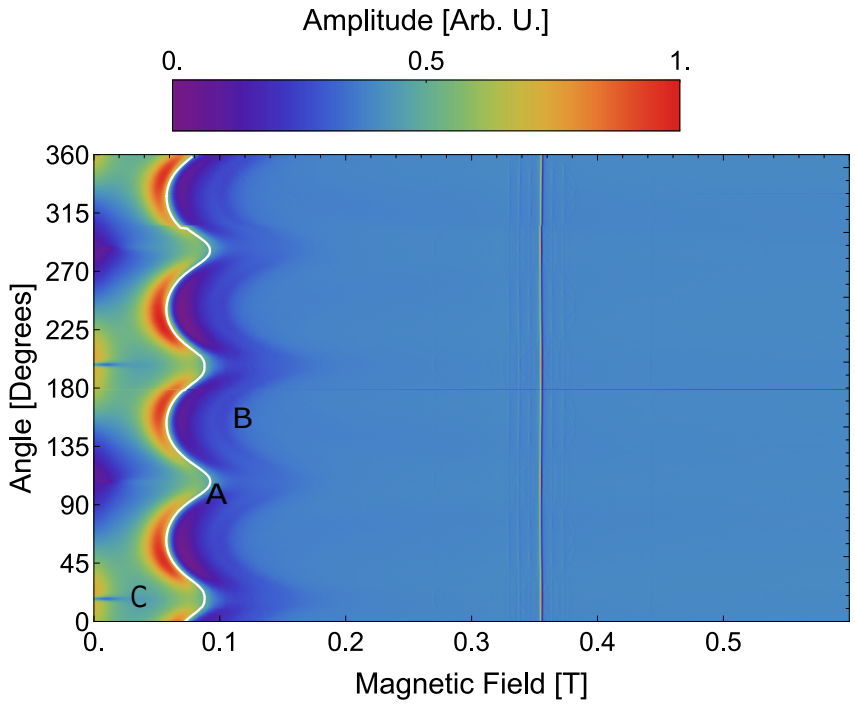

Fig. 4.4.: In-plane measurement for FeRh-2 measured with a microwave frequency of 9.8530 $\pm 10^{-5}$ GHz and a Power of 2 mW

The in-plane angular dependent measurement of FeRh-2 was performed at room temperature, with a microwave frequency of 9.5830 $\pm 10^{-5}$ GHz and a power of 2 mW. The thin film was rotated by 360° in 0.5° while the magnetic field at each angular step was swept from 0 T - 0.6 T. The measurement is shown as a colour diagram in Fig. (4.4).
The resonance position of the main signal **A** was obtained by fitting the signal with a derived Dyson function Eq.(3.2). It is visible in the colour diagram as a white line. The main signal **A** of FeRh-2 is approximately in the range of 0.05 T - 0.09 T. A cubic anisotropy is present, which produces the fourfold symmetry with 4 maxima and 4 minima. The absolute maximum of the resonance field is (0.993 $\pm 1 \cdot 10^{-4}$) T at an angle of 107° $\pm$ 0.5°, another maximum has the resonance field (0.092 $\pm 1 \cdot 10^{-4}$) T at 287.5° $\pm$ 0.5°, these maxima are here called 1^{st} order maxima. Similar to FeRh-1, there is an additional uniaxial anisotropy that reduces the value of the maxima every 180°. These smaller 2^{nd} order maxima are in the ranges 19° $\pm$ 0.5° with (0.0879 $\pm 1 \cdot 10^{-4}$) T and (197° $\pm$ 0.5 °) with (0.0878 $\pm 1 \cdot 10^{-4}$) T. This suggests that there may be a secondary signal, but unlike FeRh-1, there is no apparent 8-fold symmetry, which arises from the superposition of the signals. There are only 2 minima between (90° - 135°) in the area around 0 T, which may indicate a secondary signal.
The broadening of the 2^{nd} order maxima are similar to FeRh-1, but in attenuated form and without subordinate maxima. Within the minima **C** of a possible secondary signal there are also strong jumps in amplitude, seen at the narrow change of green, blue, green in the angular range of 15° - 22°. This behaviour is periodic with a repetition every 90°. In addition to the main signal, one further signal **B** with fourfold symmetry can be seen, which lies in the range of 0.1 T - 0.2 T. It therefore relies on cubic anisotropy. Due to the shape and position of this signal, this is referred to as the shoulder signal, shown in Fig.(A.2).

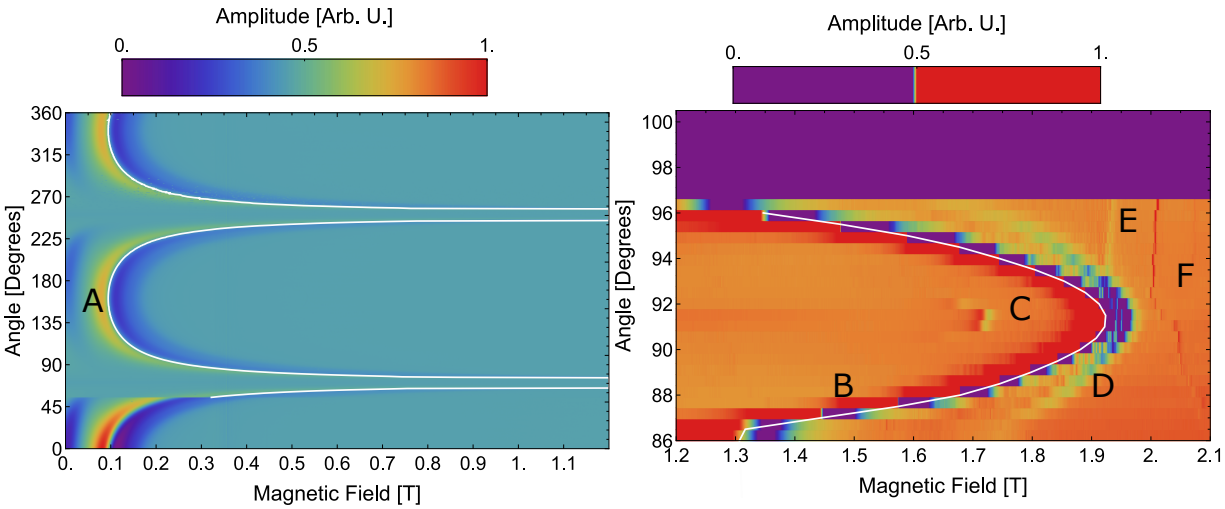

(a) FeRh-2 out-of-plane

(b) FeRh-2 out-of-plane measured in high field

Fig. 4.5.: FeRh-2 out-of-plane colour diagram, in combination with its hard axis in high fields

The resonance position of this signal can not be determined by an automatic fit due to a strong asymmetry.
The image is distorted in the range 180° and 300°, this distortion has its origin in the exclusion of erroneous measurements. In the case of 300°, a shift in the MgO signal at 0.36 T also appears. This is the result of a jump in the frequency of the microwaves.
Due to a higher fluence and therefore bigger distortion in one direction, the secondary signal of FeRh-1-in-plane could have been developed into the additional signal, which is the shoulder of FeRh-2-in-plane, with a cubic anisotropy.

FeRh-2 out-of-plane measurement

The out-of-plane measurement is shown in the colour diagram Fig. (4.5a). The microwaves had a frequency of 9.8737 ± 10^{-5} GHz, at a power of 2 mW, a 360° angular dependence in 0.5° steps was performed. An external magnetic field of 0 T to 1.2 T was applied. The main signal **A** shows a uniaxial anisotropy with a hard axis at 71.5° ±0.5° and at 251° ±0.5°, and an easy axis at 172° ±0.5° and 352° ±0.5° with $(0.096 \pm 1 \cdot 10^{-3})$ T and $(0.093 \pm 1 \cdot 10^{-3})$ T as the resonance position. The resonance position of the hard axis must be determined by means of an HF measurement. This can be seen in Fig. (4.5b). The microwaves here have a frequency of 9.5052 ± 10^{-5} GHz at 2 mW power. The angular dependence was performed from 85 ° to 95 ° in 0.5 ° step. The resonance position of the hard axis is $(1.9236 \pm 1 \cdot 10^{-4})$ T. As with FeRh-1 out-of-plane measurement, the fitted resonance line **B** is superimposed in white with the colour diagram. In addition to the main line **B** a weak signal **C** is recognisable below **B**. This is present only in an angular range of 91° - 92° and has a maximum of $(1.72 \pm 1 \cdot 10^{-2})$ T at the same angle as the hard axis of **A**. In addition, above the main signal **A** there is another signal **D**. This has a different curvature and is visible over the full angle range from 85° to 95°. The maximum resonance position of this signal is 71.5° ± 0.5° with $(1.95 \pm 1 \cdot 10^{-2})$ T. Furthermore, the signal **D** splits into a line **E** in the area of 94° in a different direction than the signal. Together with point **F** this could be interpreted as noise. The weak signal **C** below the main signal can here be interpreted as microwave absorption by a standing spin wave. The origin of signal **D** can be magnetostatic surface spin wave.

Temperature dependent in-plane FMR measurements of FeRh-2 thin films

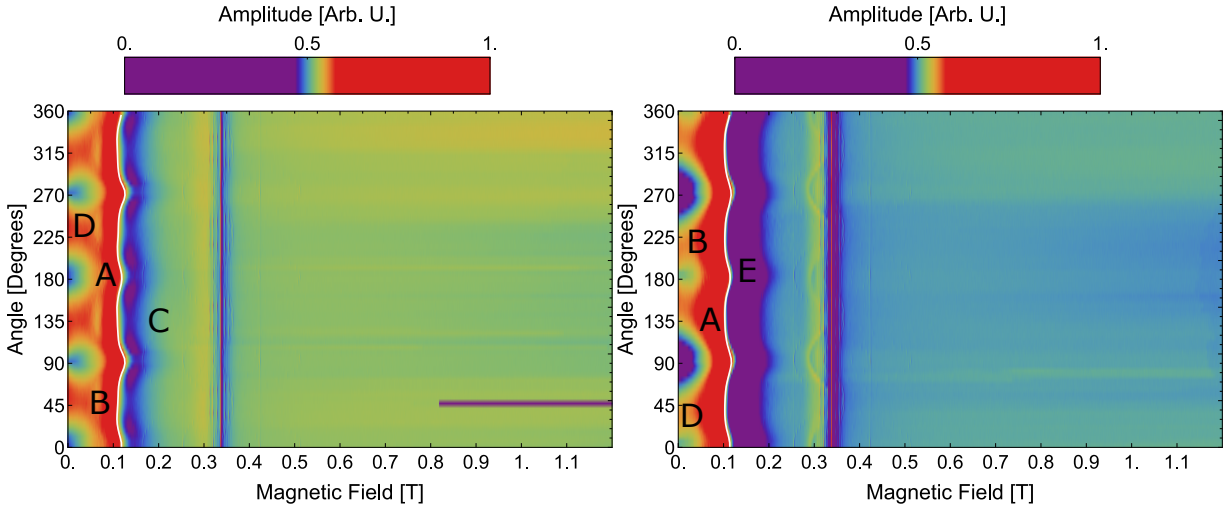

(a) FeRh-2 measured at a temperature of 100 K **(b)** FeRh-2 measured at a temperature of 200 K

Fig. 4.6.: Low temperature measurements of FeRh-2. The white line is the fit for the resonance positions

The temperature dependence was studied at temperatures of 100 K and 200 K. The microwave frequencies of both measurements are in the range 9.45 ± 10^{-3} GHz at 2 mW. The angle dependence was determined for 360° in 5° steps. During the measurement, the temperature at 100 K varied by ±0.5 K and at 200 K by ±0.5 K. The colour diagrams are visible in Fig.(4.6).
Both measurements show small angular variation of the resonance field. Therefore only a very weak cubic anisotropy **A** is visible. Each minima of the fourfold symmetry of the 100 K measurement is divided into two more minima **B**. The maxima are at angles (90°, 180°, 270°, 360° / 0°) ±5°, with one resonance position (0.125 T, 0.118 T, 0.125 T, 0.118 T) $\pm 1 \cdot 10^{-4}$T. This is also seen on a new pseudo 8-fold symmetry **C** when interpreted analogously to FeRh-1 at room temperature. Also striking are the minima **D** at a magnetic field strength of 0 T at the angles (0° / 360°, 90°, 180°, 270°). These have a circular appearance and are therefore not a direct line. In addition, they vary in amplitude, with a symmetry of 180°.
The measurement at 200 K also shows a splitting of the minima. However, a pseudo 8-fold symmetry can not to be seen here. The minima **D** are still present, but the difference in the amplitudes has risen sharply. The signals at 90° and at 270° are visible within 20°, while at 180° and 0° / 360° almost no signal is visible. The maxima of the signal are at (90°, 180°, 270°, 0° / 360°) ± 5°. Their resonance positions are (0.117 T, 0.114 T, 0.116 T, 0.133 T) $\pm 1 \cdot 10^{-3}$ T. A uniaxial anisotropy which varies the values of the maxima is thus likewise present. The difference of the maxima, however, has become smaller compared to 100 K.
A secondary signal would explain the signals **C** and **D**. Either the effective magnetisation has risen slightly from 200 K to 100 K, or the cubic anisotropy has changed. In view of the fact that 200 K has a large region **E** which has a weak signal and changes into a narrower region at 100 K, a change in cubic anisotropy is to be expected. The uniaxial anisotropy gains strength with lower temperature.

4.2. Measurements of FeRh thin films with moderate fluence

4.2.1. FeRh-3

FeRh-3-in-plane measurement

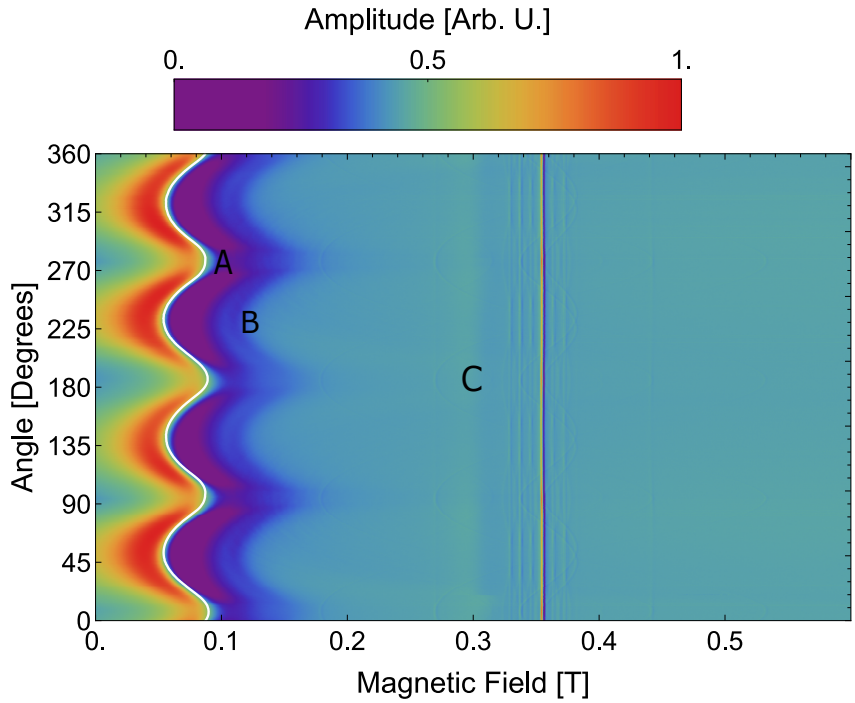

Fig. 4.7.: In-plane measurement for FeRh-3 measured with a microwave frequency of 9.8782 ± 10^{-5} GHz and a Power of 2 mW

The thin film FeRh-3 was measured in-plane at a frequency of 9.8782 ± 10^{-5} GHz and a power of 2 mW. The external magnetic field was swept from 0 T to 0.6 T. The angle ϕ was changed from 0 to 360 ° in increments of 0.5 °. The measurement is shown in Fig.(4.7).
The main signal **A** of FeRh-3 has a in-plane cubic anisotropy.The absolute maximum is 0.0898 T $\pm 1 \cdot 10^{-4}$ T at an angle of 7° $\pm$ 0.5°. Analogous to the previous thin films, FeRh-3 has an additional uniaxial anisotropy, which produces two different values for the maxima. Thus, the 2^{nd} order maximum is shifted by 90° and has a value of $(0.0872 \pm 1 \cdot 10^{-4})$ T at 98.5° $\pm$ 0.5°. Unexpectedly, this maxima is shifted by 1.5° from the expected position of 97°. The same happens with the following maximum $(0.089 \pm 1 \cdot 10^{-4})$ T at 185.5° $\pm$ 0.5°. This has a much larger shift from 3°. The fourth maximum is shifted again with $0.0871 \pm 1 \cdot 10^{-4}$ T at 277.5° $\pm$ 0.5°. It is noticeable that the shift is growing steadily with 1.5 °. Due to the monotonous slope, it can be assumed that there is a systematic error that could have resulted from the deletion of unusable data records. Like the maxima, the minima are affected by a superimposed uniaxial anisotropy. The absolute minimum here is $(0.0538 \pm 1 \cdot 10^{-4})$ T and 233° $\pm$0.5° with a further minimum of the 1^{st} order $0.054 \pm 1 \cdot 10^{-4}$ at 52.5° $\pm$ 0.5°. The minima of the 2^{nd} order are ($0.0559 \pm 1 \cdot 10^{-4}$) T and $(0.0559 \pm 1 \cdot 10^{-4})$ T at 143.5° $\pm$ 0.5° and 321.5° $\pm$ 0.5°. Again, the angles differ widely. A shift caused by an altered crystal symmetry may be ruled out, otherwise this error would have the same values symmetrically to 90° or 180°.

In addition to the main signal, a second signal **B** is visible again. This signal, here called shoulder, has a cubic anisotropy superimposed with uniaxial anisotropy. However, this superposition is not as pronounced as it is the case with the main signal **A**. Due to the similar shape and positioning between 0.1 T and 0.2 T, the same assumptions apply as with FeRh-2 in-plane measurements. With an external magnetic field of 0.3 T, an additional signal **C** is recognisable in this measurement, this has a large linewidth ΔH and shows no angular dependence. The assumption is therefore obvious that it is an EPR signal from the sample holder or contamination in the cavity.

FeRh-3 out-of-plane measurement

The out-of-plane angular dependence of FeRh-3 FMR signal is shown in Fig. (4.8a). Microwaves with a frequency of 9.8782 $\pm 10^{-5}$ GHz and a power of 2 mw were used. The thin film was rotated 360° in 0.5° steps. The external magnetic field was varied from 0 T to 1.2 T. The main signal **A** shows a uniaxial anisotropy with a resonance field at hard axis exceeding 1.2 T. The easy axis is 180° $\pm$0.5° and 359.5° $\pm$ 0.5° with resonance positions (0.0629 $\pm 1 \cdot 10^{-4}$) T and (0.063 $\pm 1 \cdot 10^{-3}$) T. To determine the maxima it is necessary to use the HF setup, the results can be seen in Fig.(4.8b). The HF measurement was carried out at microwave frequencies of 9.5059 $\pm 10^{-5}$ GHz with 2 mw power. The magnetic field was changed from 1.2 T to 2.1 T and the angle from 75° to 85° in 0.5° increments. The white line is the fitted resonance position of signal **A/B**. This signal has an hard axis with a resonance field of (1.918 $\pm 1 \cdot 10^{-3}$) T. Another signal **C** can be found below the main signal with a resonance field of (1.74 $\pm 1 \cdot 10^{-2}$) T. Similar to FeRh-2 out-of-plane scan, this signal can be traced back to a standing spin wave within the thin film. In addition, signals **D** and **E** are visible. Signal **D** is greater than 1.9 T and shows a weak angle dependence, it can be assumed that this is just noise during the measurement.

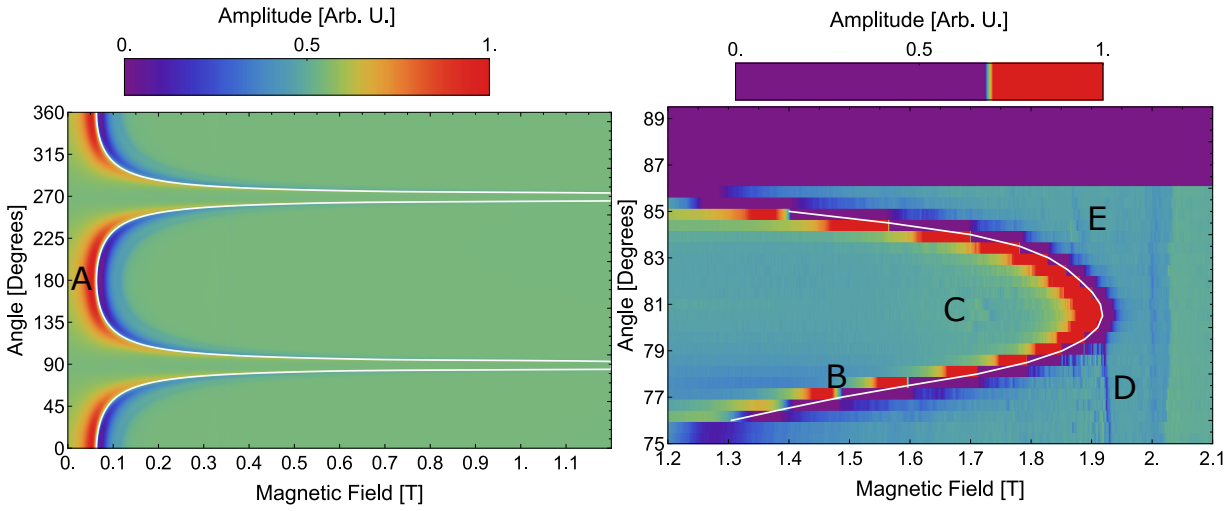

(a) FeRh-3 out-of-plane

(b) FeRh-3 out-of-plane measured in high field

Fig. 4.8.: Complete out-of-plane measurements of FeRh-3

Temperature dependent in-plane FMR measurements of FeRh-3 thin films

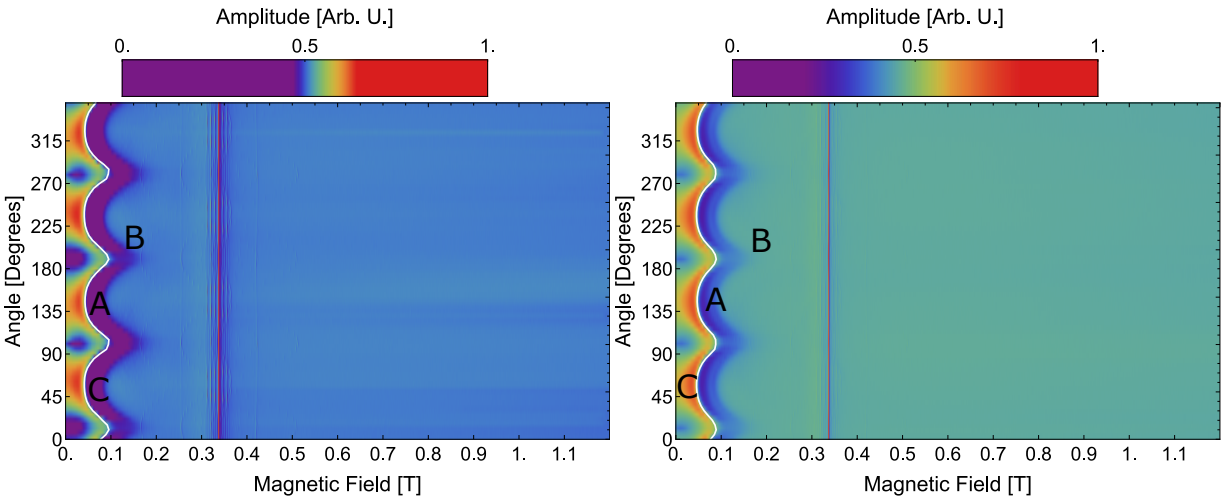

(a) FeRh-3 measured at a temperature of 100 K **(b)** FeRh-3 measured at a temperature of 200 K

Fig. 4.9.: Low temperature measurements of FeRh-3

The measurement for FeRh-3 was done from 100 K to 450 K in 100 K increments, except for 300 K. All colour diagrams are shown in Fig.(4.9) and Fig.(4.10). The frequencies of all measurements are very close, so that a frequency of 9.542 ± 10^{-5} GHz $\pm$ 10^{-3} GHz is assumed. In addition, the microwaves had a power of 2 mw in each measurement. The angular increments for 100 K and 200 K are 5°, while 450 K and 400 K have 4° steps for the 360° angle dependency. For all measurements, the external magnetic field was varied from 0 T to 1.2 T.
Measurements 100 K and 200 K were obtained in a different setup as 400 K and 450 K. Therefore they vary in the positioning on the sample holder, thus the easy and the hard axis for 100 K and 200 K stays the same, the same applies to 400 K and 450 K. The values of resonance field can be seen in the Table (4.2) and Table (4.3).
The main signal **A** of each measurement shows a cubic anisotropy. The easy axis of 100 K and 200 K are available at angle (60°, 145°, 235°, 325°). For 100 K and 200 K, the hard axis is at angles (10°, 105°, 190°, 285°).
Point **B** marks a maximum which has a smaller resonance field than the maxima above or below **B**. It is noticeable that the reduced maxima appear brighter at (10°, 190°). This could be a sign of a superposition with a secondary signal. Point **C** indicates minima for an external field from 0 T to 0.5 T. These minima appear at 100 K and increase when they are at the reduced maxima **B**. The minima **C**, which lie with larger resonance fields have a smaller radius. This could be another indication of a secondary signal. The 200 K measurement has also differences in the minima **C**. In addition, the difference of the maxima is bigger than at 100 K.

Table 4.2.: Maxima of the resonance field at the hard axis for 100 K, 200 K, 400 K and 450 K

Angle [± 5°]	10	105	190	285	Angle [± 4°]	28	120	212	300
100 K [$\pm 1 \cdot 10^{-4}$ T]	0.0953	0.0955	0.0951	0.0953	400 K [$\pm 1 \cdot 10^{-4}$ T]	0.0854	0.0829	0.0850	0.0834
200 K [$\pm 1 \cdot 10^{-4}$ T]	0.0889	0.0879	0.0890	0.0879	450 K [$\pm 1 \cdot 10^{-4}$ T]	0.0875	0.0845	0.0868	0.0854

Table 4.3.: Minima of the resonance field at the easy axis for 100 K, 200 K, 400 K and 450 K

Angle [± 5°]	60	145	235	325	Angle [± 4°]	76	164	256	344
100 K [$\pm 1 \cdot 10^{-4}$ T]	0.0412	0.0427	0.0411	0.0424	400 K [$\pm 1 \cdot 10^{-4}$ T]	0.0639	0.0651	0.0638	0.0652
200 K [$\pm 1 \cdot 10^{-4}$ T]	0.0457	0.0469	0.0456	0.0471	450 K [$\pm 1 \cdot 10^{-4}$ T]	0.0714	0.0722	0.0722	0.0731

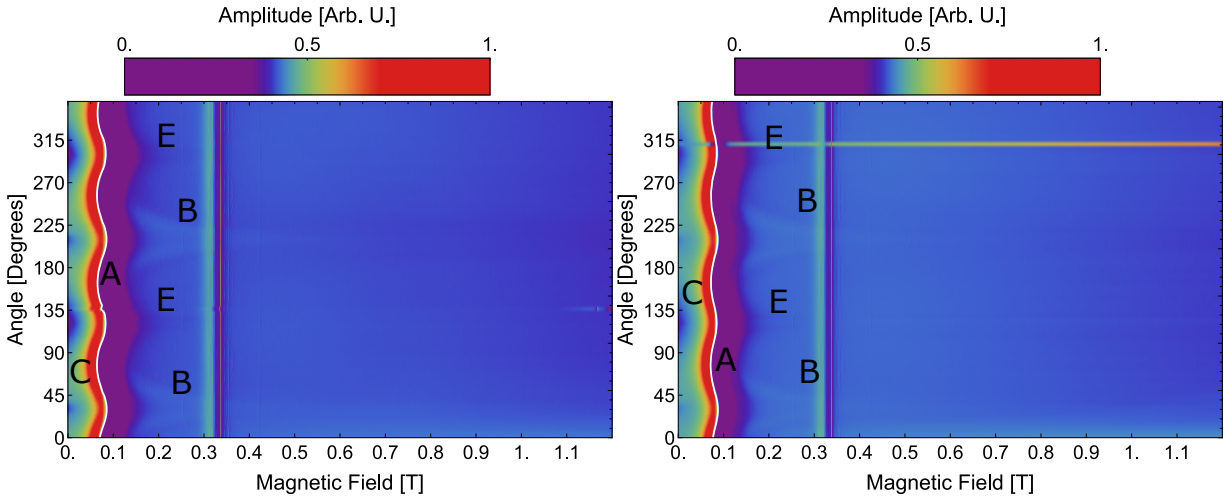

(a) FeRh-3 measured at a temperature of 400 K **(b)** FeRh-3 measured at a temperature of 450 K

Fig. 4.10.: High temperature measurements of FeRh-3

The measurements at 400 K and 450 K have hard axis at (28°, 120°, 212°, 300°), the corresponding resonance fields can be found in Table (4.2). These measurements also show different values for the maxima. However, at 400 K, another signal **B** is formed for the first time at the angle of reduced maxima (120°, 300°). At these angles, the already weak signal **C** almost vanishes completely. For 450 K the signal **B** is more pronounced, it seems to have a resonance field at hard axis greater than 1.2 T. With higher fields it gets an additional weak signal. The signals **C** completely disappear at angles of signal **B**, while having a weak signal in the range of the normal maxima. In addition, these maxima form another signal **E**. This resembles the horizontal line from FeRh-1 or the horizontal line from the out-of-plane measurements.
As the temperature increases, the effective magnetisation increases. This is visible as a shift to higher fields, increasing from 100 K to 450 K. This effect is very weak. Investigations at temperatures higher than 450 K are not possible, because there is a risk of annealing the thin films, so that their disordered crystal lattice gets ordered.

4.2.2. FeRh-4

FeRh-4-in-plane measurement

The in-plane measurement of FeRh-4 is shown in Fig. (4.11). It was measured with a microwave frequency of 9.8767 ± 10^{-5} GHz and a power of 2 mw in an angle range of 0° - 360° in 0.5° steps. A magnetic field was swept from 0 T to 0.6 T.
The signal of FeRh-4 in-plane shows a superposition of the cubic anisotropy **A** with a uniaxial

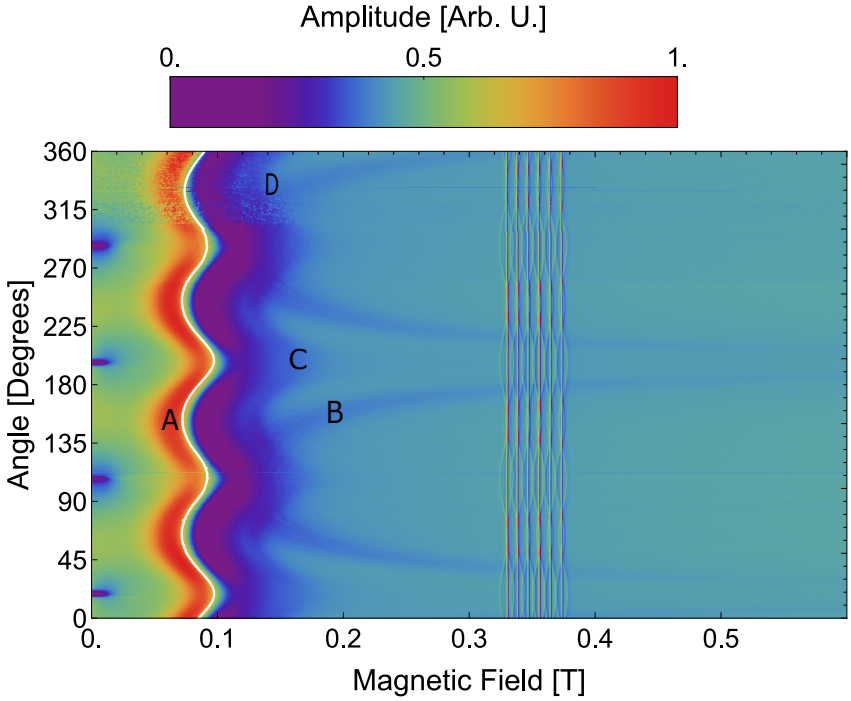

Fig. 4.11.: In-plane measurement for FeRh-4 performed with a microwave frequency of 9.8767 ± 10^{-5} GHz and a power of 2 mw, with an angle increment of 0.5°

anisotropy **B**. This overlay causes the periodic differences in the maxima and minima. Again, a distinction is made between 1^{st} and 2^{nd} order. The 1^{st} order maxima are the absolute maximum $(0.0973 \pm 1 \cdot 10^{-4})$ T at 19° ± 0.5° and $(0.0972 \pm 1 \cdot 10^{-4})$ T at 198.5° ± 0.5°. The 2^{nd} order maxima are at $(0.092 \pm 1 \cdot 10^{-4})$ T with 109.5° ± 0.5° and $(0.0918 \pm 1 \cdot 10^{-4})$ T at 286° ±1°. The 1^{st} order minima are the absolute minimum $(0.0716 \pm 1 \cdot 10^{-4})$ T at 62.3° ± 0.5° and $(0.0717 \pm 1 \cdot 10^{-4})$ T at 244.5° ± 0.5°. The 2^{nd} order minima are at $(0.0721 \pm 1 \cdot 10^{-4})$ T with 154.5° ± 0.5° and $(0.0738 \pm 1 \cdot 10^{-4})$ T with 329° ±1°.
The deviations of the angles are in the range of the errors, only the 2^{nd} order minimum of 329° ±1° lays outside the error bar. However, this can be attributed to the strong noise **D** in the angular range of 300°-360°. The noise could be caused by an excessive gas flow of the nitrogen that interrupts the tuning of the cavity.
The assumption made for in-plane measurement of FeRh-1, that a superposition of a secondary signal **B** with uniaxial anisotropy is present, can be confirmed by FeRh-4. This initially assumed signal is now clearly visible in the range 0.1 T to 0.6 T and marked as **B**.
The easy axis is superimposed with the maxima of 2^{nd} order, which could explain the low values. The resonance at hard axis of this signal lies outside the considered range from 0 T to 0.6 T. FeRh-4 in-plane scan also shows the previously observed shoulder **C**. The assumption that the shoulder **C** is the secondary signal has not been confirmed, otherwise one of the signals **B** or **C**

should have vanished. Another approach to the origin of these signals is that they both originated from ion irradiation but are based on different effects. Thus, the shoulder **C** could be the result of the disorder of Ne^+-ion irradiation and the consequent emergence of a sub-lattice of the crystal. So far only FeRh-1-in-plane shows no shoulder, which can be attributed to the low fluence. The additional secondary uniaxial signal, as already suspected, may be an effect of the direction of irradiation, and would explain why this has only a uniaxial and no cubic anisotropy.

FeRh-4 out-of-plane measurement

The out-of-plane measurement for FeRh-4 is shown in Fig. (4.12a). The microwaves had a frequency of 9.8777 ± 10^{-5} GHz with a power of 2 mw. The external magnetic field was swept in a range of 0 T to 1.2 T. The angle has been changed by 360° in 0.5° step. The main signal **A** shows a uniaxial symmetry with a hard axis at 86.5° ± 0.5° and 267° ± 0.5° with a resonance field higher than 1.2 T. The easy axis is at 176.5° ± 0.5° and 357.5° ±0 , 5° with a resonance field $(0.098 \pm 1 \cdot 10^{-3})$ T and $(0.098 \pm 1 \cdot 10^{-3})$ T. An HF measurement was made to determine the resonance positions at the hard axis. In this case, the microwaves had a frequency of 9.5134 ± 10^{-5} GHz at a power of 20 mw. The angular dependence was measured from 99° to 112° in 0.25° increments. The HF signal **B**, in Fig.(4.12b), shows a resonance position at $(1.795 \pm 1 \cdot 10^{-3})$ T. In addition, again a signal **C** appears below the main signal **B**. This has a maximum resonance field of $(1.59 \pm 1 \cdot 10^{-3})$ T at 86.5° ± 0.5°. This has the same shape as the previous signals below the main line, so can be assumed as a standing spin wave. Another signal is **D**. This is reminiscent of (4.5b point E) from FeRh-2 out-of-plane angular measurement. This also goes from the maximum and approaches the value 1.8 T with increasing angle. The amplitude of this signal decreases until the end of the measurement, at 112°.

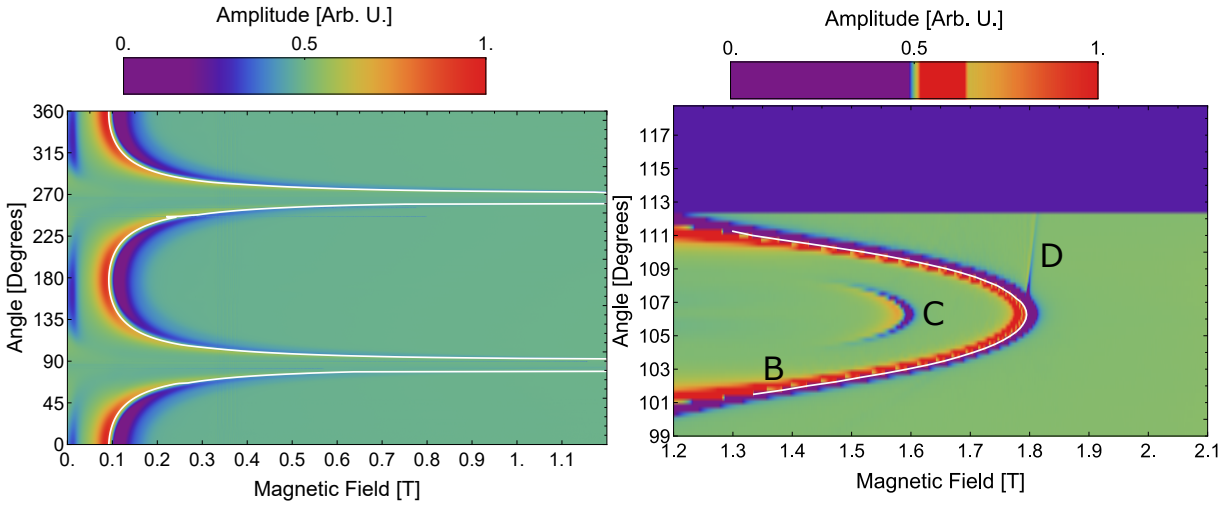

(a) FeRh-4 out-of-plane

(b) FeRh-4 out-of-plane measured in high field

Fig. 4.12.: FeRh-4 complete out-of-plane angular dependence

4.3. Measurements of FeRh thin film with high fluence

4.3.1. FeRh-5

FeRh-5 in-plane measurement

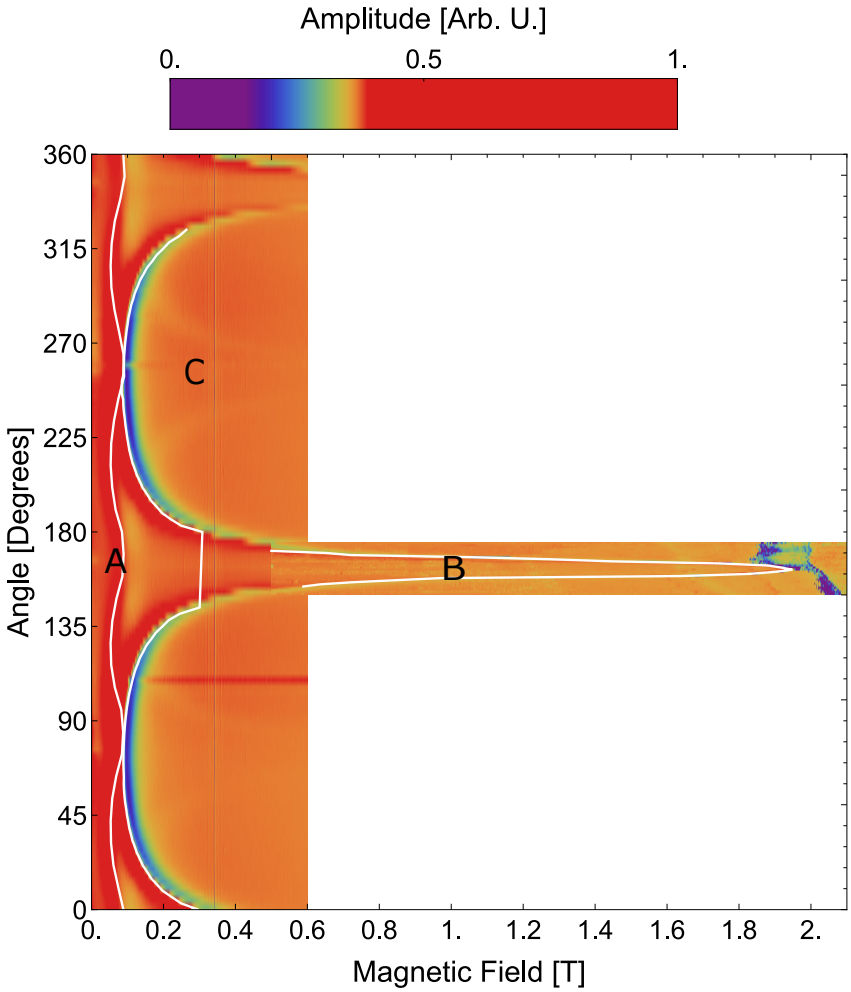

Fig. 4.13.: In-plane measurement for FeRh-5 measured with a microwave frequency of 9.5077 ± 10^{-5} GHz and a Power of 2 mw with an angle increment of 1°. This diagram is a composition of two different measurements. The measurement for signal **B** took place with a frequency of 9.5076 ± 10^{-5} GHz, a power of 20 mW and an increment of 1°.

The measurement was carried out with a frequency of 9.5077 ± 10^{-5} GHz and a power of 2 mW. Two different magnetic field strengths were chosen. One measurement was from 0 T to 0.6 T, the other could only be achieved with the HF setup and had a range of 0.5 T to 2.1 T. The combined measurements are shown in Fig. (4.13).
Most notable, here is the prominent secondary signal with uniaxial anisotropy with a hard axis **B**. The hard axis extends to a resonance field of $(1.9483 \pm 1 \cdot 10^{-4})$ T at $162° \pm 1°$. The main signal **A** with cubic anisotropy of FeRh is still visible, but here the secondary signal **B** is of equal amplitude. An automatic, computer-implemented fit of the main signal **A** with its fourfold symmetry could not be performed because the superposition with the secondary signal in the ranges of 45° - 90° and 250° - 300° is too big.
It seems that the uniaxial signal **B** in FeRh-5 in-plane measurement is the main signal rather

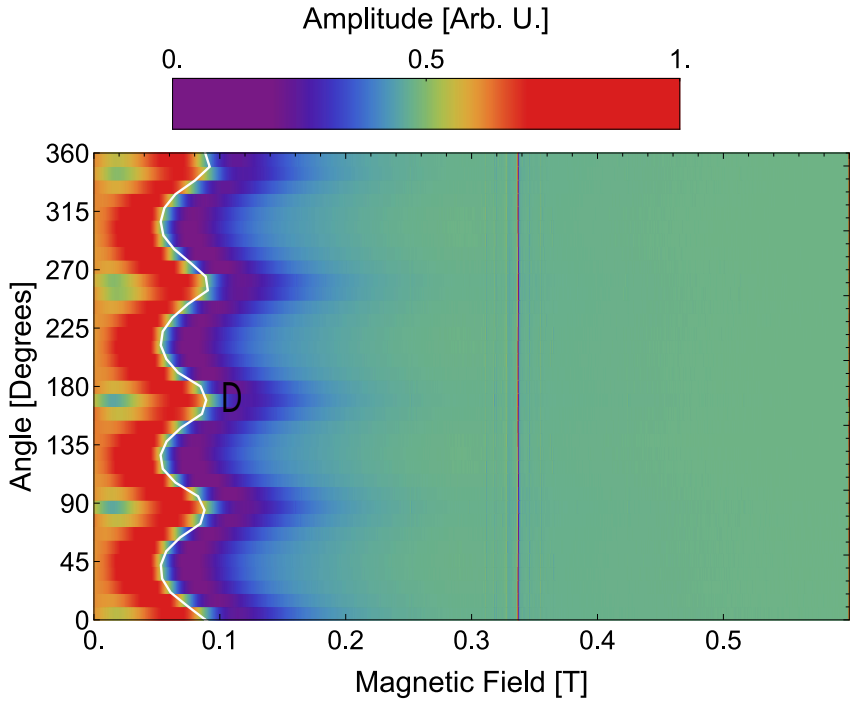

Fig. 4.14.: Quasi in-plane measurement for FeRh-5 measured with a microwave frequency of 9.3016 ± 10^{-5} GHz and a power of 20 mw with an angle increment of 10°, by means of the two-axis goniometer

than the cubic signal **A**. In the ranges 45° - 100° and 225°-300° an additional very weak signal **C** is visible which also has a high resonance field in the hard axis, which goes beyond 0.6 T. This signal shows a uniaxial anisotropy shifted by 45° to the uniaxial main signal **B**. However, cubic anisotropy can not be ruled out because **B** could cover the extra cubic parts. The shoulder of the previous thin films is no longer visible.
This thin film was measured twice, the result was always the same and thus reproducible. In addition, another measurement was taken on a larger piece of FeRh-5. This shows the same angular dependence. Thus, the large signal **B** is not a specific effect of the thin film used and also no due to the effect of alignment error inside the cavity.
For further investigations, a two-axis goniometer was used. This allowed the variation of both θ and ϕ angle. The idea behind this measurement is to rotate θ in the direction of the hard axis and then obtain an angular dependence by varying ϕ. This measurement is shown in Fig. (4.14). This shows an FeRh main signal with cubic anisotropy **D**, the secondary signal is completely gone. The assumption is obvious that the thin film was not perfectly aligned parallel to the external magnetic field, since the positioning of the angle θ was done by eye. By extracting the resonance line of this measurement and superimposing it on the colour diagram, the superimposed FeRh main signal **A** becomes visible.
The extracted signal has a cubic anisotropy with no additional uniaxial anisotropy. The shift of the maxima of the fourfold signal is due to the manual positioning of the thin film on the sample holder and the associated error. This raises the question why the large uniaxial signal is visible only in correct positioned in-plane direction. An explanation could be related to the direction of oscillation of the magnetic part of the microwaves. The disorder due to irradiation is only generated on the surface of the thin films and does not penetrate very deep into the crystal lattice. Using the two-axis goniometer, the thin film is placed in the out-of-plane direction. However, with an out-of-plane sample holder, it is also possible to position the thin film in an in-plane

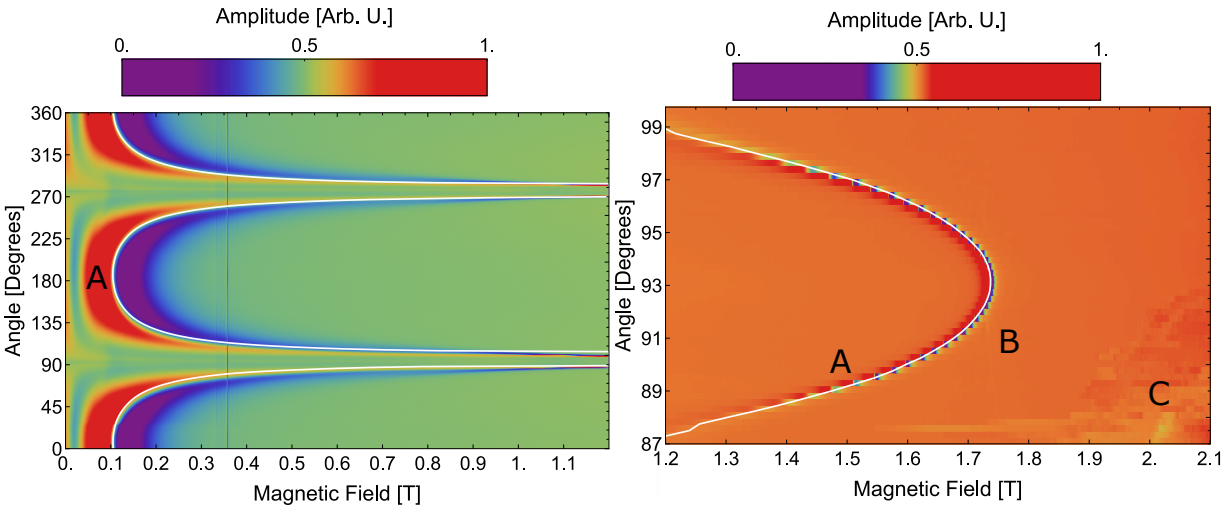

(a) FeRh-5 out-of-plane

(b) FeRh-5 out-of-plane measured in high field

Fig. 4.15.: Complete out-of-plane measurements of FeRh-5

direction. This is when the external magnetic field is applied parallel to the thin film surface. The two-axis goniometer can then perform a ϕ angular dependence in this in-plane position. This special in-plane positioning increases the penetration depth of the magnetic component of the microwaves. Now that the lower layers of the FeRh contribute to the FMR signal, the disorder-induced uniaxial signal could be overlaid. The bigger contribution of the inner unirradiated layers of the FeRh thin film is also the reason why the signal of the out-of-plane measurements is many times greater than the signal in in-plane measurements.
The origin of the large uniaxial signal and its sensitivity in the direction of θ is currently unknown and could not be further investigated within the framework of this bachelor thesis due to the limited time.

FeRh-5 out-of-plane measurement

The out-of-plane measurement of FeRh-5 was taken at a frequency of 9.835 ± 10^{-4} GHz at 2 mW. The magnetic field was varied from 0 T to 1.2 T for 360° in 1° increments. It is shown in Fig.(4.15a).
The main signal **A** shows a uniaxial anisotropy with an hard axis at 91° ±1° and 272° ±1°. The minima of the main signal are at 7° ±1° and 18° ±1° with resonance positions of (0.104 $\pm 1 \cdot 10^{-3}$) T and (0.104 $\pm 1 \cdot 10^{-3}$) T. A HF measurement at a frequency of 9.5077 ± 10^{-5} GHz and power of 20 mw was performed to determine the resonance position of the hard axis. It is visible in Fig.(4.15b). The resonance for the hard axis is therefore at (1.737 $\pm 1 \cdot 10^{-3}$) T for an angle of 91° ±1°. The standing spin wave signal below the main signal has disappeared, which might be due to different magnetisation of FeRh-5 thin film.
Another weak signal **B** can be seen slightly below the maximum at 1.72 T . This has also been observed in previous measurements. Thus, it could be a resonance signal and not noise. However, the origin is unknown. Furthermore, in **C** a large noise signal can be seen, which extends in a wide range from 1.6 T to 2.1 T.

4.3.2. FeRh-6

FeRh-6-in-plane measurement

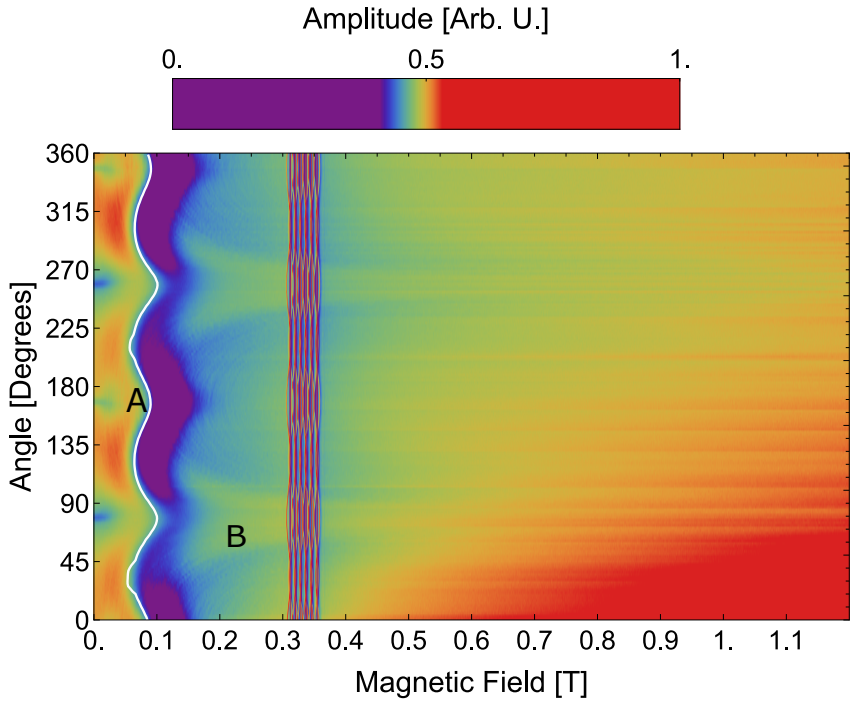

Fig. 4.16.: In-plane measurement for FeRh-6 measured with a microwave frequency of 9.4264 ± 10^{-5} GHz and a power of 20 mw

The thin film FeRh-6 was measured at a frequency of 9.4264 ± 10^{-5} GHz with a power of 20 mw in in-plane direction. The angle ϕ was rotated in 2° steps by 360 °. A sweep of the external magnetic field from 0 T to 1.2 T was carried out per step. The colour diagram of FeRh-6-in-plane is visible in Fig.(4.16)
The FeRh main signal **A** lies in the range of 0.05 T - 0.15 T and has a cubic anisotropy superposed with a uniaxial anisotropy. The maxima can be subdivided into first and 2^{nd} order. The 1^{st} order maxima are $(0.1 \pm 1 \cdot 10^{-3})$ T at 258° ±2° and $(0.10 \pm 1 \cdot 10^{-3})$ T at 78° ±2°, the second highest with $(0.09 \pm 1 \cdot 10^{-3})$ T at 166° ±2° and $(0.09 \pm 1 \cdot 10^{-3})$ T at 348° ±2°. The absolute minimum is $(0.053 \pm 1 \cdot 10^{-3})$ T at 30° ±2° the other $(0.056 \pm 1 \cdot 10^{-3})$ T at 159° ±2°, $(0.064 \pm 1 \cdot 10^{-3})$ T at 235° ±2° and $(0.064 \pm 1 \cdot 10^{-3})$ T at 338° ±2°.
Starting from the large difference of the maxima, the in-plane uniaxial anisotropy $K_{2\parallel}$ will be bigger compared to other thin films. The reduced difference between minima and maxima will also result in a smaller value $K_{4\parallel}$ of the cubic anisotropy.
The maxima of 2^{nd} order are broadened here analogously to FeRh-1. Unlike FeRh-1 the secondary signal **B** is visible. It has a uniaxial anisotropy with a resonance field at hard axis that goes beyond 0.6 T. The linewidth ΔH of this signal becomes broad at higher fields starting at 0.4 T, so that the signal **B** almost disappears. This secondary signal **B** is not as dominant than the uniaxial signal of FeRh-5-in-plane and is therefore reminiscent of the shoulder signal of FeRh-2, FeRh-3 and FeRh-4. It would be conceivable that the irradiation in FeRh-6 combines the separated effects, especially since FeRh-6 has the highest fluence. Meaning that, the direction of irradiation promotes the formation of a sub-lattice which has a uniaxial symmetry in the direction of irradiation that is separate from the cubic symmetry of the FeRh lattice.

FeRh-6 out-of-plane measurement

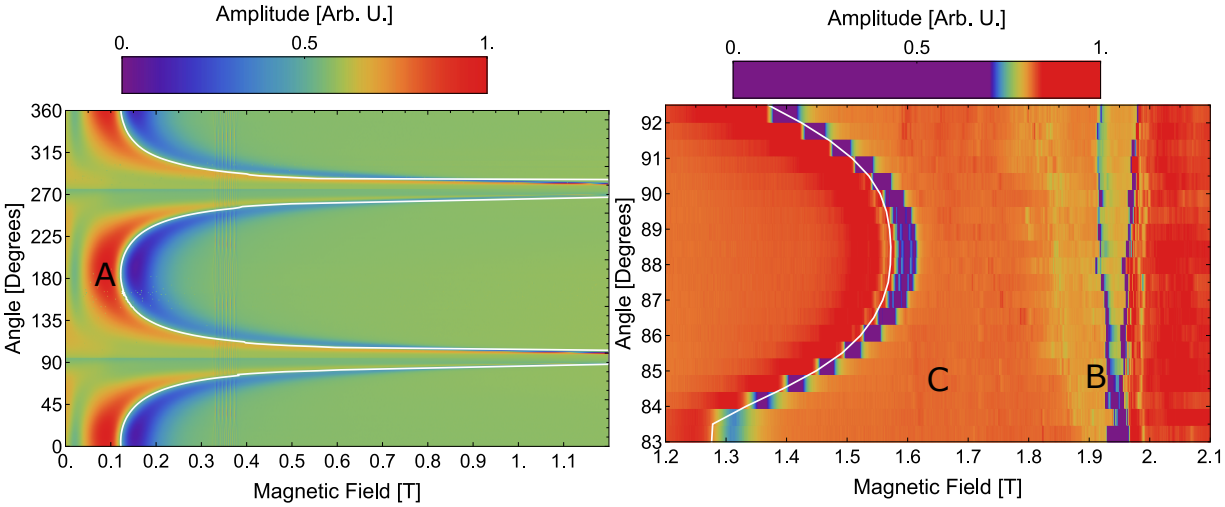

(a) FeRh-6 out-of-plane

(b) FeRh-6 out-of-plane measured in high field

Fig. 4.17.: Complete out-of-plane measurements of FeRh-6

The measurement was carried out for a microwave frequency of 9.8675 ± 10^{-5} GHz at 2 mW power and is shown in Fig. (4.17a). The angular dependence was performed for magnetic field strengths from 0 T to 1.2 T in 360° for 1° steps. The main signal **A** obtained has a uniaxial anisotropy.
The easy axis with its minima is at $(0.122 \pm 1 \cdot 10^{-3})$ T and $(0.122 \pm 1 \cdot 10^{-3})$ T for angles from 0° ±1° and 185° ±1°. In order to be able to completely determine the hard axis of the uniaxial signal **A**, a HF measurement with a microwave frequency of 9.4476 ± 10^{-5} GHz and a power of 20 mw was carried out. This measurement is shown in Fig. (4.17b) as a colour diagram. The considered angular range included 83° to 93° in 0.5°, with the magnetic field varied from 1.2 T to 2.1 T. The main signal has a resonance position at the hard axis at $(1.572 \pm 1 \cdot 10^{-3})$ T for angles 92° ±1° and 274° ±1°.
One notices the white lines at the maximum of signal **A**. These were caused by noise at the lowest position of the signal. The noise starts at a field strength of 1.5 T at an angle of 85° ± 0.5° and stops at 92° ± 0.5°. Compared to other high-field measurements, FeRh-6 out-of-plane measurement has the strongest noise, with a large signal **B** between 1.9 T and 2 T. Signal **B** is divided into two signals whose distance increases with increasing angle. In addition, the previously observed signal **C** can be seen near the maxima. It can now finally be assumed that this is a resonance signal and not noise. A standing spin wave is not visible. The general line shape of this main signal is highly asymmetric to the highest, so that up to 70% of the amplitude is below the signal without resonance.

Table 4.4.: The left column shows the resonance field maxima of the hard axis. The right column shows the resonance field minima of the easy axis. The values of the hard axis are values obtained from a fit whose resonance position was constrained to about 1.2 T. As one can see all values are near to 1.2 T, which means they are not representing the real hard axis.

Angle [± 4°]	176	356	88	268
350 K [$\pm 1 \cdot 10^{-4}$ T]	0.1144	0.115	0.0763	0.0768
400 K [$\pm 1 \cdot 10^{-4}$ T]	0.1171	0.1177	0.0782	0.0788
450 K [$\pm 1 \cdot 10^{-4}$ T]	0.1205	0.1205	0.0794	0.0787

Temperature dependent in-plane FMR measurements of FeRh-6 thin films

The temperature measurement of FeRh-6 was performed for 350 K, 400 K and 450 K, it is shown in Fig.(4.18). The temperature had a fluctuation of $\Delta T = \pm 0.1$ K. The frequencies are 9.4530 ± 10^{-5} GHz for 350 K, 9.4479 ± 10^{-5} GHz for 400 K and 9.4506 ± 10^{-5} GHz for 450 K. All measurements were carried with one setup, thus the positioning of the thin film did not change. Therefore the hard and easy axis stays at the same angle. The values can be found in Table (4.4).

The measured signals show a strong uniaxial anisotropy **A** with a hard axis at angle 167° and 356°. The resonance positions are not known because the hard axis is above 1.2 T and the measurement covers only the range 0 T to 1.2 T. The signal **B** has an amplitude greater than the background and also shows a two-fold symmetry. As the temperature rises, signals **A** and **B** become sharpened. The minima with 0 T at 90° as well as 270° get bigger from 350 K at 400 K, while they get smaller at 450 K.

Beginning with 400 K, another minimum forms in the easy direction of signal **A**. This signal **C** is recognisable at 450 K. It splits the easy axis in half. One presumption is that this is the missing cubic anisotropy of the FeRh, which was initially superimposed but now becomes apparent as the uniaxial signal weakens. The latter is recognisable by the distribution of the colour scale, which shifts closer to the minimum at 450 K.

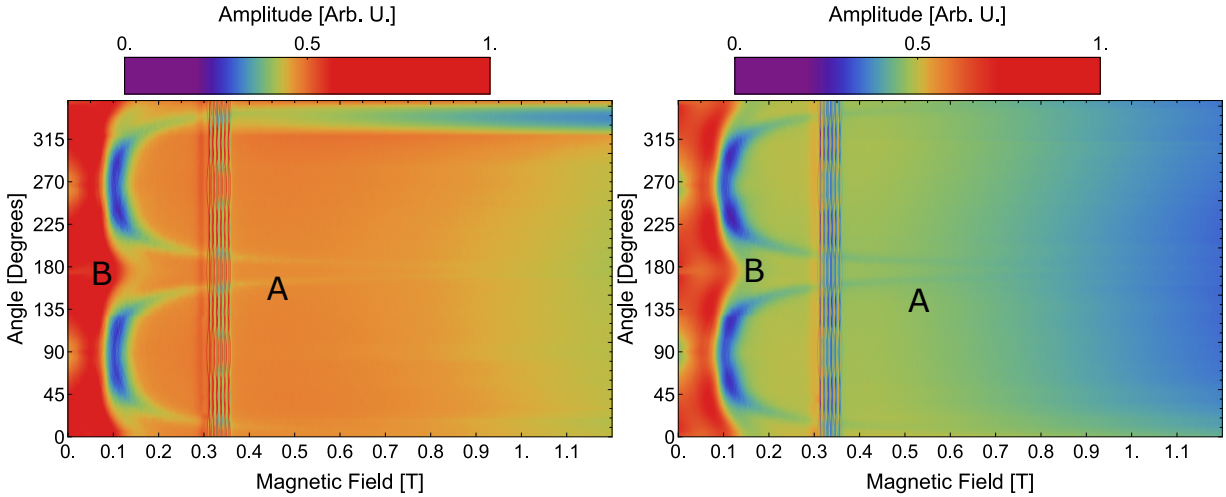

(a) FeRh-6 measured at a temperature of 350 K **(b)** FeRh-6 measured at a temperature of 400 K

Fig. 4.18.: Moderately high temperature measurements of FeRh-6

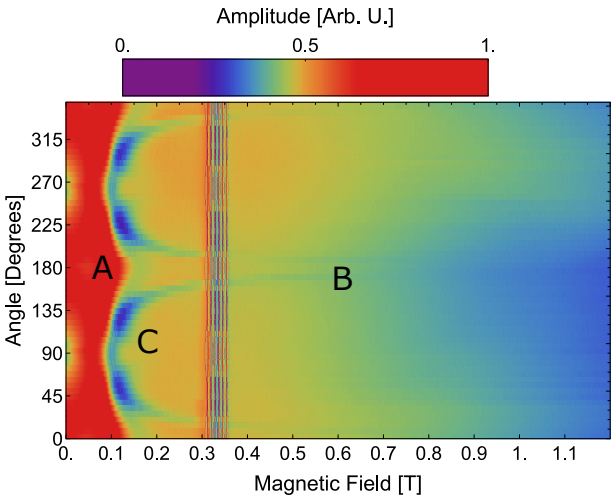

Fig. 4.19.: FeRh-6 measured at a temperature of 450 K

4.4. Analysis of the anisotropy of FeRh

At the beginning, a small overview of the anisotropy of the temperature measurements. These could not be fully evaluated due to lack of time and are therefore only described.
Both FeRh-1 and FeRh-2 show similar behaviour. Their cubic anisotropy becomes smaller with lower temperatures, this is well visible on FeRh-2 at 200K Fig.(4.6b). In addition, the uniaxial signal becomes more recognisable. However, comparing this behaviour with FeRh-3 and FeRh-6 reveals a completely different result.
Here the behaviour is exactly the other way round. The cubic anisotropy of FeRh-3 increases to the maximum at 100K. This can be seen in the large difference between minima and maxima, which becomes lower with increasing temperature. The uniaxial signal is only recognisable at a temperature of 400K and becomes stronger with increasing temperature.
FeRh-6 shows analogies to FeRh-3, here already at 350K a very strong uniaxial signal is visible. This shows a weak loss of intensity as the temperature rises. In addition, at a high temperature of 450K, the cubic signal appears as an superimposition with the uniaxial signal. At this point, it can be stated that at very low fluences, the temperature dependence of the anisotropy is exactly mirrored to the behaviour at higher fluence.
FeRh-1 and FeRh-2 have the lowest fluences studied here, with $1 \cdot 10^{13}$ Ions / cm^2 and $2 \cdot 10^{13}$ Ions / cm^2. The thin film with superior fluence is FeRh-3. It has a fluence five times higher than FeRh-2. In the area between these two fluences, therefore, a change in the anisotropy must occur. In addition, the lowest fluences have a temperature hysteresis, which would allow them to be in a different phase at lower temperatures.

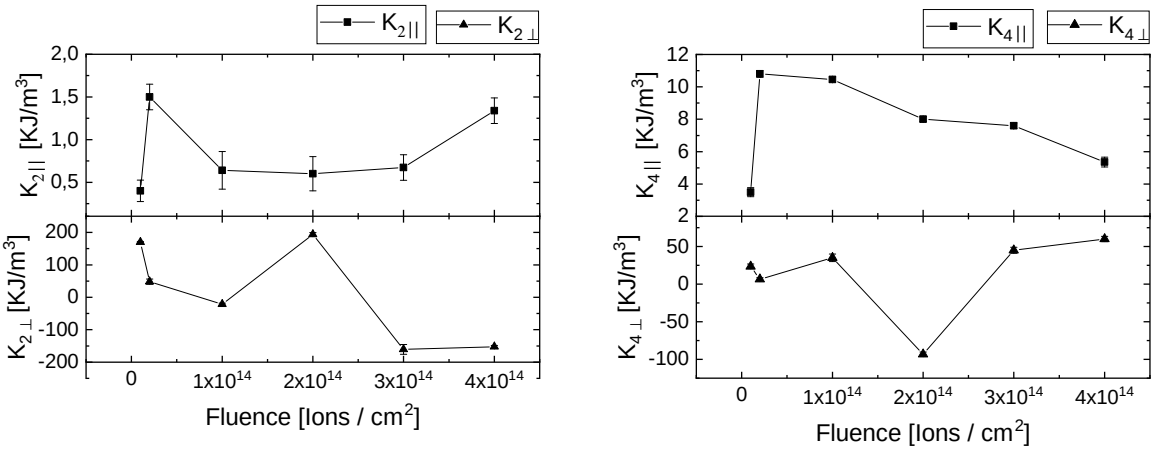

(a) Uniaxial constants $K_{2\perp}$ and $K_{2\parallel}$, displayed in one plot

(b) Cubic constants $K_{4\perp}$ and $K_{4\parallel}$, displayed in one plot

Fig. 4.20.: Anisotropy constants plotted versus the fluence

From the fitted resonance curves, the anisotropy constants can now be extracted. These constants are shown in Table (4.5). For every thin film a g-factor of 2.05 was assumed, which was obtained through frequency dependent measurements [19]. In addition, these values can be plotted over the fluence, in order to reveal the course of the anisotropy with increasing fluence. The constant $K_{2\perp}$ is shown together with $K_{2\parallel}$ in Fig. (4.20a). It is visible, that the value of $K_{2\perp}$ drops with increasing fluence. Noticeable is the jump of FeRh-4. Looking at the graph as a whole, $K_{2\perp}$ falls with increasing fluence, with FeRh-4 as an exception. From FeRh-3 to FeRh-6, $K_{2\perp}$ is negative. The minimum is -160.67 $\pm$ 15 kJ / m^3 for FeRh-5. The slope after FeRh-6 is smaller than from FeRh-3 to FeRh-5. In combination with the large error of FeRh-5, a plateau forming at FeRh-5 can also be assumed.
On the other hand, the minimum of $K_{2\parallel}$ is 0.4 $\pm$ 0.12 kJ /m^3 at FeRh-1. Nevertheless $K_{2\parallel}$ shows a big jump to the maximum of 1.5 $\pm$ 0.15 kJ /m^3 at FeRh-2. The overall progression falls to 0.6 $\pm$ 0.2 kJ /m^3 for FeRh-4, followed by a second maximum FeRh-6 at 1.335 $\pm$ 0.15 kJ /m^3. A large constant $K_{2\parallel}$ means a bigger difference between the maxima. This is a first indicator of superposition with a secondary uniaxial signal. It therefore makes sense that $K_{2\parallel}$ increases for large fluences, as these thin films show a particular signal. More surprising is, that FeRh-4 represents the minimum. However, this could also be a result of the big $K_{2\perp}$. With a maximum difference of 34%, $K_{2\parallel}$ has the biggest error in this analysis.
Figure (4.20b) shows the constant $K_{4\parallel}$ and $K_{4\perp}$ of cubic and tetragonal anisotropy. The constant $K_{4\parallel}$ decreases with increasing fluence. It has a maximum at 10.46 $\pm$ 0.15 kJ /m^3 for FeRh-2. The absolute minimum is FeRh-1 with 3.5 $\pm$ 0.27 kJ /m^3. This behaviour can also be observed in the in-plane measurements. There, the difference between minimum and maximum decreases with increasing fluence. The cubic anisotropy would thus have to be lower. Furthermore, a low cubic anisotropy for FeRh-1 was already assumed in Ch.(4.1.1) and could now be confirmed.
For $K_{4\perp}$ the absolute minimum is FeRh-4 with -93.32 $\pm$ 0.3 kJ /m^3. The overall shape of this graph shows a rising $K_{4\perp}$, with a maximum at FeRh-6 with 60 $\pm$ 0.35 kJ /m^3.
The origin of the jump for FeRh-4 $K_{4\perp}$ and $K_{2\parallel}$ could lay in the formation of a more pronounced tetragonal distortion. These would change $K_{2\perp}$, $K_{4\parallel}$ and $K_{4\perp}$. A tetragonal distortion can explain why FeRh-4 has a large $K_{2\perp}$ and a negative $K_{4\perp}$. Looking at F_{tet}, $K_{4\perp}$ and $K_{4\parallel}$ are subtracted from $K_{2\perp}$, with negative $K_{4\perp}$, F_{tet} is magnified. In the case of FeRh-4 this results in a large tetragonal deformation. This also happens in the case of FeRh-3, FeRh-5 and FeRh-6, when $K_{2\perp}$ is negative, certainly F_{tet} gets negative due to a positive $K_{4\perp}$.

From $K_{2\perp}$ the effective magnetic field M_{eff} can be derived, which together with the saturation magnetisation M_S is shown in Fig. (4.21). In the course of high fluences M_{eff} drops, with a negative slope to 1.28 T. A absolute minimum is FeRh-1 with 0.979 T. Due to a big jump to the next point, a big error can be assumed.

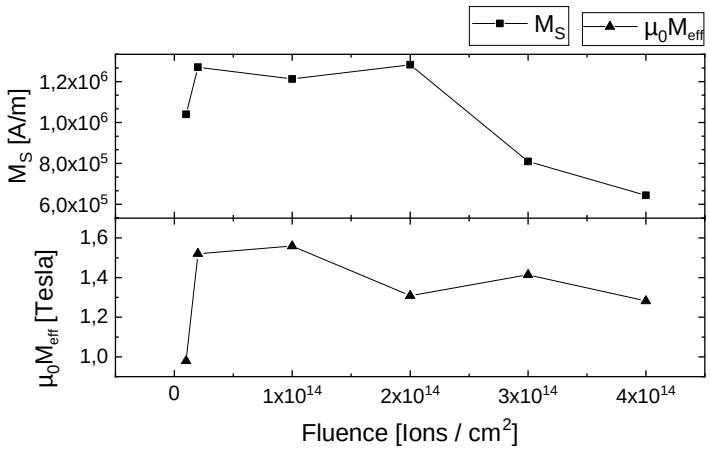

Fig. 4.21.: Saturation magnetisation and effective magnetisation plotted versus the fluence

Compared to the ordered FeRh thin films of Mancini et al. [30], visible in Table (4.5), constants $K_{2\parallel}$ and $K_{4\parallel}$, of the irradiated thin films differ in an acceptable range to the unirradiated. Constant $K_{2\perp}$ and $K_{4\perp}$ show no relation to Mancini's constants. Therefore one has to assume an error in the determination of both. For $K_{2\perp}$ every thin film shows a big difference of up to $\pm 680\,\mathrm{kJ/m^3}$, while $K_{2\parallel}$ stays in an acceptable range. $K_{4\perp}$ also shows a big difference, comparable with the difference of $K_{2\perp}$. On the other hand, the constant $K_{4\parallel}$ shows a maximum difference of about $\pm 5\,\mathrm{kJ/m^3}$.
One should also notice, that the saturation magnetisation of Mancinis unirradiated 50nm FeRh thin film is higher than M_S of FeRh-1, FeRh-5 and FeRh-6.

Table 4.5.: Anisotropy constants of the FeRh thin films and the constants of Mancini et al. [30].

Thin film	Fluence [Ions / cm^2]	g-factor	$K_{2\perp}$ [kJ / m^3]	$K_{2\parallel}$ [kJ / m^3]	$K_{4\perp}$ [kJ / m^3]	$K_{4\parallel}$ [kJ / m^3]	ϕ_U	M_S [A / m]	$\mu_0 M_{eff}$ [T]
FeRh-1	$1 \cdot 10^{13}$	2.05	170 ± 2	0.4 ± 0.12	23.59 ± 3.2	3.5 ± 0.27	2.38 ± 0.1	1.04E6	0.97
FeRh-2	$2 \cdot 10^{13}$	2.05	48 ± 8	1.5 ± 0.15	6.58 ± 0.2	10.8 ± 0.2	2.4 ± 0.1	1.27E6	1.52
FeRh-3	$1 \cdot 10^{14}$	2.05	-21.2 ± 3.1	0.64 ± 0.22	35 ± 0.5	10.46 ± 0.15	3.57 ± 0.4	1.213E6	1.48
FeRh-4	$2 \cdot 10^{14}$	2.05	194 ± 5.5	0.6 ± 0.2	-93.32 ± 0.3	8 ± 0.15	2 ± 0.1	1.282E6	1.31
FeRh-5	$3 \cdot 10^{14}$	2.05	-160.67 ± 15	0.67 ± 0.15	44.4 ± 0.4	7.59 ± 0.17	0.74 ± 0.1	809000	1.41
FeRh-6	$4 \cdot 10^{14}$	2.05	-152.27 ± 3.5	1.335 ± 0.15	60 ± 0.35	5.35 ± 0.3	2.51 ± 0.11	644000	1.28
Mancini	0	2.05 ± 0.06	520 ± 10	0.73 ± 0.16	0.0023 ± 0.008	6.4 ± 1	/	1.16E6 ± 0,015E6	1.122 ± 0.001

5. Conclusions and outlook

The anisotropy of ion-disordered FeRh thin films changes significantly with increasing fluence, although the disorder of the crystal lattice is merely superficial. Thus, with increasing fluence, additional non-predicted signals were formed, which can show cubic as well as uniaxial anisotropy. This extends the contemplation of the anisotropy from an original cubic signal to many different signals. Furthermore the temperature measurements indicate a change of anisotropy with different magnetic phases, to be seen in the completely different behaviour at low fluence and high fluence, for low and high temperatures.
Further investigations must now be carried out in order to be able to characterise the thin films more accurately. Thus, the temperature dependence for all films has to be determined. These include supplementary measurements such as the FeRh-6 low temperature measurement. Likewise, the in-plane hard axis of the uniaxial signals should be determined analogously to FeRh-5. These values can then be used to reduce an error in the fit of the anisotropy constant. If necessary, the thin films with very large deviations should be measured again. Alternatively, further thin films can be made that have a fluence in the vicinity of these anomalies, like FeRh-4 or between FeRh-2 and FeRh-3 to get a better understanding of this temperature dependent anisotropy.
In order to better evaluate and understand the influence of the disordered crystal lattice on the thin films, it would be appropriate to characterise their surfaces. This can be done by AFM as well as MFM.
Another influence on the results has the age of the thin films. Since these do not have a protective layer, oxidation, which has an effect on the saturation magnetisation, can not been ruled out. The saturation magnetisation should therefore be checked by means of a SQUID measurement. Alternatively, an in-situ FMR measurement would be suitable.
Furthermore, films with higher fluence than those considered here, can be made to follow the resulting signals.
An interesting result is the measurement of FeRh-5 in-plane using the two-axis goniometer. Further measurements, to rule out a positioning error inside the cavity, should be made. The two-axis goniometer should also find its use in FeRh-4 and FeRh-6. These have, analogous to FeRh-5, a strong uniaxial signal and would be predestined for this use.

A. Appendix

A.1. Plots

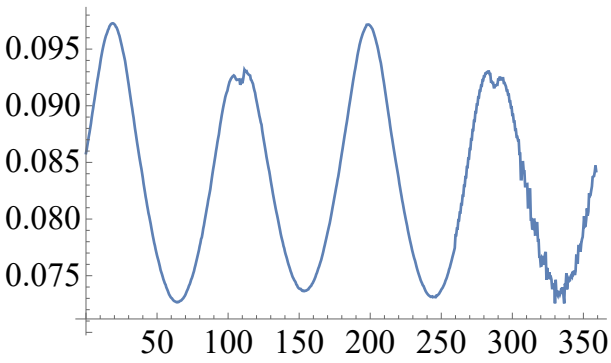

Fig. A.1.: Fit of the resonance position for FeRh-4 in-plane. One can see the different heights of the maxima

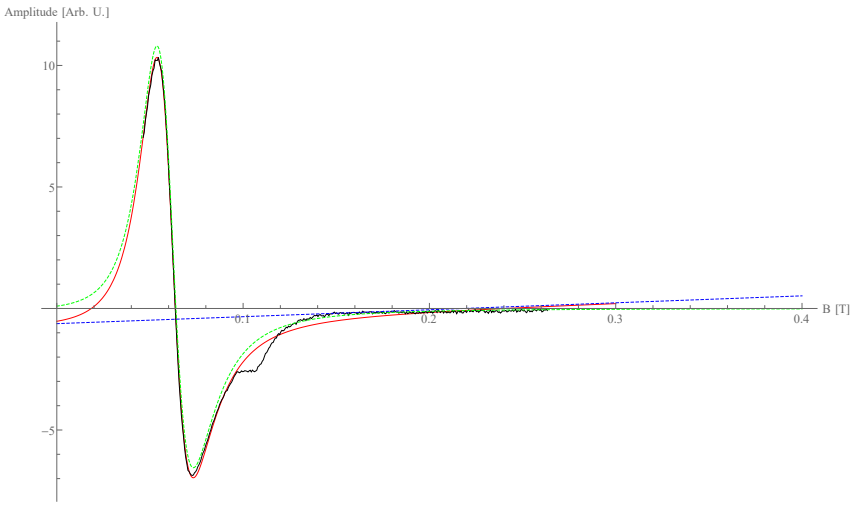

Fig. A.2.: In-plane signal of FeRh-2 between 0 T and 0.3 T with the mentioned shoulder at 0.1 T. Black is the data obtained from the measurements, the green dashed line is one Dyson derivative and the blue dashed line is a linear function to correct a possible offset.

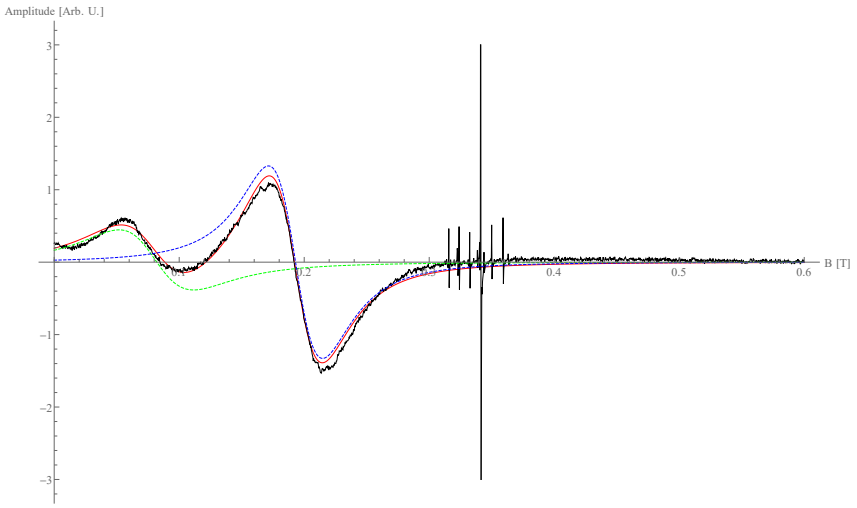

Fig. A.3.: In-plane fit for FeRh-5 between 0 T and 0.6 T. The signal below 0.1 T has a cubic anisotropy, the signal at about 0.2 T shows a uniaxial anisotropy

A.2. Free energy density/ potential landscape

A short visual description of how each anisotropy constant is affecting the free energy density.

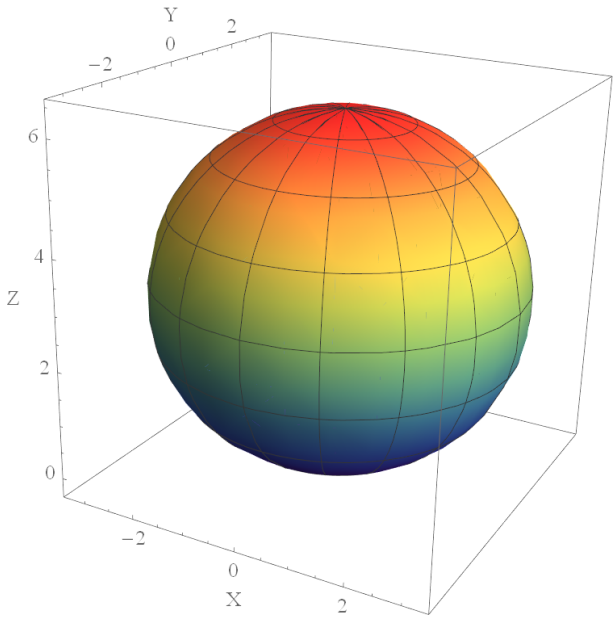

Fig. A.4.: No anisotropy means, the potential landscape is a sphere. The magnetisation can move in any direction, without the need of spending work. It therefore has no easy- or hard axis.

A.2.1. Uniaxial

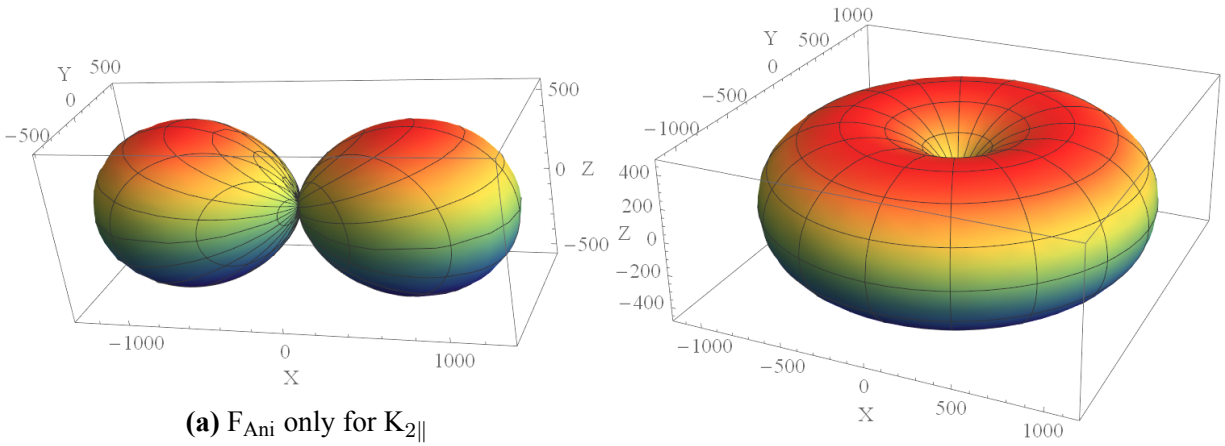

(a) F_{Ani} only for $K_{2\parallel}$

(b) F_{Ani} only for $K_{2\perp}$

Fig. A.5.: The uniaxial anisotropy only affects the energy density on one axis

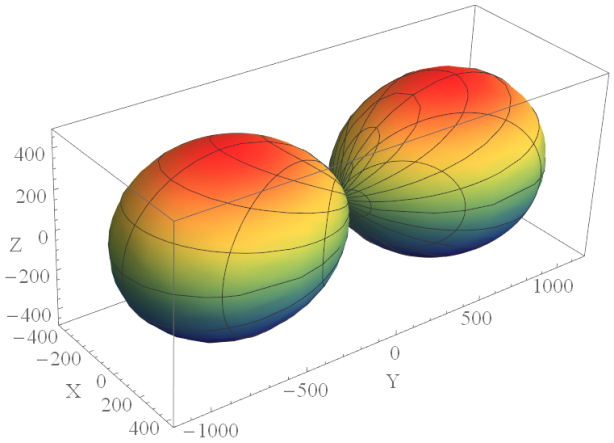

Fig. A.6.: Combination of the uniaxial contributions. The hard axis here is the direction of propagation. Here only in one direction. The easy axis, here it would be an easy plane,is in the middle.

A.2.2. Cubic

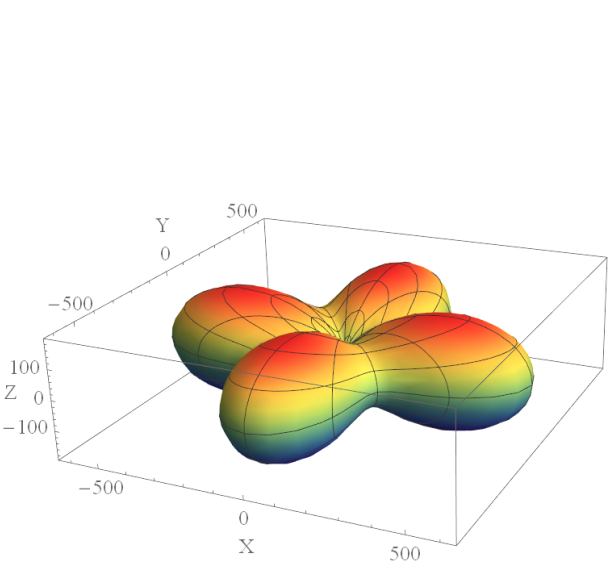

(a) F_{Ani} only for $K_{4\parallel}$

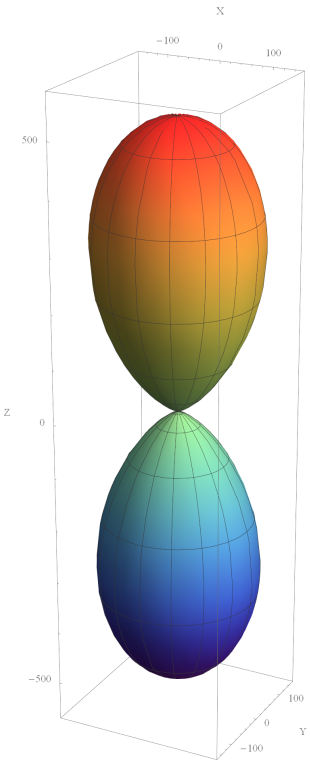

(b) F_{Ani} only for $K_{4\perp}$

Fig. A.7.: The cubic anisotropy only affects the energy density in two axes

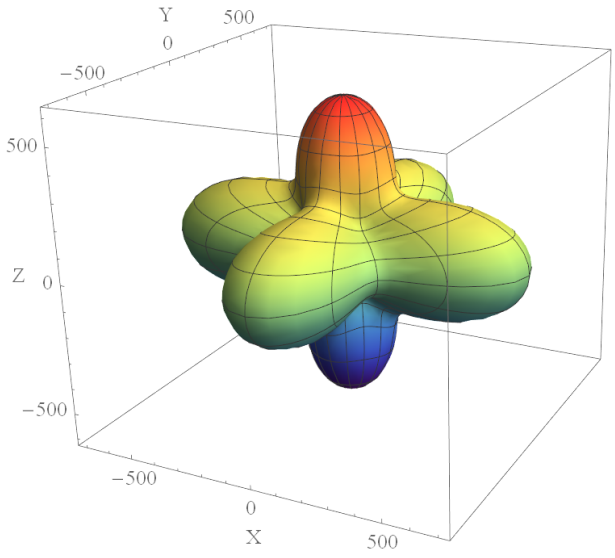

Fig. A.8.: Combination of the cubic contributions. The cubic anisotropy affects F_{Ani} in every cubic direction, which means on two axes in in-plane (parallel) and one axis in perpendicular direction. The hard axis is visible as the maxima of F_{Ani} in 6 directions. In the X-Y-plane the easy axis is located between the maxima.

A.2.3. Free energy density for FeRh-2

With the results obtained for FeRh-2 in Ch.(4.4) one can look at F_{Ani} of an FeRh thin film.

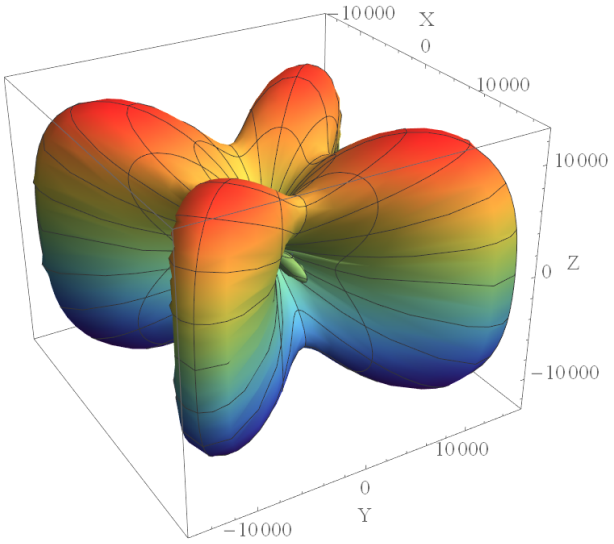

Fig. A.9.: F_{Ani} for FeRh-2. The cubic anisotropy is visible in four directions. An additional uniaxial anisotropy is visible as narrower wing, which is only present in an 180° symmetry. The pillar in the middle could be the signal visible at 0T. It has big jumps, thus needs to be very narrow, as can be seen in the plot.

A.3. Open questions

This bachelor thesis has generated more questions than could be answered. Following is a list of open questions.

In view of the appearance of an additional uniaxial anisotropy, the question of the origin arises.

Does this signal depend on the used irradiation angle and the irradiation direction? How far does the secondary signal interfere with the performed fits?

The measurement with the two-axes goniometer shows a very sensitive θ dependence, why?

Why does only the uniaxial signal disappear?

Can these results of FeRh-5 in-plane be achieved with other thin films?

From FeRh-2 the additional signal appears, where is the origin of this and why does it disappear with FeRh-1, as well as FeRh-5 and FeRh-6? What are the signals, that appear in a small to no external magnetic field and why do they have large jumps in the amplitude within a few degrees?

Could an imperfectly smooth surface of MgO cause a change in anisotropy, that affects the comparison between the thin films?

Can one reach the Curie temperature before annealing, if yes, where is this?

Why does the anisotropy change its behaviour in the temperature measurements from FeRh-2 to FeRh-3 and from FeRh-3 to FeRh-6?

What does the surface of the thin films look like, is it possible to recognise another crystal structure?

List of Figures

2.1. Sphercial coordinates, used to describe the free enthalpy. θ_H and ϕ_H are the angles corresponding to $\vec{H}$, while θ and ϕ represent the magnetsiation $\vec{M}$. The image was taken from [9]. 5

3.1. Schematic illustration of EPR system (Elexsys-II-E500). A cylindrical cavity is mounted without additional pole pieces 8
3.2. Schematic illustration of the microwave bridge 9
3.3. Elexsys-II-E500 Schematic with pole pieces **E**. The place for the cavity got narrower, therefore the rectangular Varian cavity, which is smaller in diameter, needs to be mounted 11
3.4. Rutherford Back-Scattering of the FeRh samples after the magnetron sputtering [19] 12
3.5. Temperature dependence of magnetisation of FeRh irradiated with different fluence [19] 13
3.6. Thermally induced phase transition from the antiferromagnetic phase to the ferromagnetic phase. In the AF-Phase the rhodium atoms have no magnetic moment, whilst they contribute to the magnetisation in the FM-phase 14
3.7. Nucleation of ferromagnetic or antiferromagnetic domains in FeRh while heating or cooling. The phase transition temperature differs depending if one is cooling or heating the thin film. The nucleation of domains of the corresponding phases begins after exceeding the current phase transition temperature. The figure was taken from Mancini et al. [30] 15

4.1. In-plane angular dependent FMR of FeRh-1 displayed in a colour plot; measured at f = 9.4567 $\pm 10^{-5}$ GHz and microwave power of 20 mW 17
4.2. The high field measurement was done, in order to catch the hard axis. For this the setup was changed, to reach a magnetic field of 2.1 T 19
4.3. The measurements for 100 K and 200 K were done in one session, that is why their angles are corresponding to the same axes. The white line is the fit for the resonance positions 19
4.4. In-plane measurement for FeRh-2 measured with a microwave frequency of 9.8530 $\pm 10^{-5}$ GHz and a Power of 2 mW 20
4.5. FeRh-2 out-of-plane colour diagram, in combination with its hard axis in high fields 21
4.6. Low temperature measurements of FeRh-2. The white line is the fit for the resonance positions 22
4.7. In-plane measurement for FeRh-3 measured with a microwave frequency of 9.8782 $\pm 10^{-5}$ GHz and a Power of 2 mW 23
4.8. Complete out-of-plane measurements of FeRh-3 24
4.9. Low temperature measurements of FeRh-3 25
4.10. High temperature measurements of FeRh-3 26

4.11. In-plane measurement for FeRh-4 performed with a microwave frequency of 9.8767 ± 10^{-5} GHz and a power of 2 mw, with an angle increment of 0.5° . . . 27
4.12. FeRh-4 complete out-of-plane angular dependence . . . 28
4.13. In-plane measurement for FeRh-5 measured with a microwave frequency of 9.5077 ± 10^{-5} GHz and a Power of 2 mw with an angle increment of 1°. This diagram is a composition of two different measurements. The measurement for signal **B** took place with a frequency of 9.5076 ± 10^{-5} GHz, a power of 20 mW and an increment of 1°. . . . 29
4.14. Quasi in-plane measurement for FeRh-5 measured with a microwave frequency of 9.3016 ± 10^{-5} GHz and a power of 20 mw with an angle increment of 10°, by means of the two-axis goniometer . . . 30
4.15. Complete out-of-plane measurements of FeRh-5 . . . 31
4.16. In-plane measurement for FeRh-6 measured with a microwave frequency of 9.4264 ± 10^{-5} GHz and a power of 20 mw . . . 32
4.17. Complete out-of-plane measurements of FeRh-6 . . . 33
4.18. Moderately high temperature measurements of FeRh-6 . . . 34
4.19. FeRh-6 measured at a temperature of 450 K . . . 35
4.20. Anisotropy constants plotted versus the fluence . . . 36
4.21. Saturation magnetisation and effective magnetisation plotted versus the fluence 37

A.1. Fit of the resonance position for FeRh-4 in-plane. One can see the different heights of the maxima . . . 39
A.2. In-plane signal of FeRh-2 between 0 T and 0.3 T with the mentioned shoulder at 0.1 T. Black is the data obtained from the measurements, the green dashed line is one Dyson derivative and the blue dashed line is a linear function to correct a possible offset. . . . 39
A.3. In-plane fit for FeRh-5 between 0 T and 0.6 T. The signal below 0.1 T has a cubic anisotropy, the signal at about 0.2 T shows a uniaxial anisotropy . . . 40
A.4. No anisotropy means, the potential landscape is a sphere. The magnetisation can move in any direction, without the need of spending work. It therefore has no easy- or hard axis. . . . 40
A.5. The uniaxial anisotropy only affects the energy density on one axis . . . 41
A.6. Combination of the uniaxial contributions. The hard axis here is the direction of propagation. Here only in one direction. The easy axis, here it would be an easy plane,is in the middle. . . . 41
A.7. The cubic anisotropy only affects the energy density in two axes . . . 42
A.8. Combination of the cubic contributions. The cubic anisotropy affects F_{Ani} in every cubic direction, which means on two axes in in-plane (parallel) and one axis in perpendicular direction. The hard axis is visible as the maxima of F_{Ani} in 6 directions. In the X-Y-plane the easy axis is located between the maxima. . 42
A.9. F_{Ani} for FeRh-2. The cubic anisotropy is visible in four directions. An additional uniaxial anisotropy is visible as narrower wing, which is only present in an 180° symmetry. The pillar in the middle could be the signal visible at 0T. It has big jumps, thus needs to be very narrow, as can be seen in the plot. . . . 43

List of Tables

3.1. Anisotropy constants for an ordered FeRh thin film with 50 nm thickness,according to Mancini et al. [30] 14

4.1. FeRh thin films sorted by the used fluence, the corresponding saturation magnetisation M_S and overall area, beginning with the unirradiated and ending at the most irradiated thin film. Everything was measured at room temperature. . 16
4.2. Maxima of the resonance field at the hard axis for 100 K, 200 K, 400 K and 450 K 26
4.3. Minima of the resonance field at the easy axis for 100 K, 200 K, 400 K and 450 K 26
4.4. The left column shows the resonance field maxima of the hard axis. The right column shows the resonance field minima of the easy axis. The values of the hard axis are values obtained from a fit whose resonance position was constrained to about 1.2 T. As one can see all values are near to 1.2 T, which means they are not representing the real hard axis. 34
4.5. Anisotropy constants of the FeRh thin films and the constants of Mancini et al. [30]. 37

Bibliography

[1] Vitalij K. Pecharsky and Karl A. Gschneidner Jr. “Magnetocaloric effect and magnetic refrigeration”. In: *Journal of Magnetism and Magnetic Materials* 200.1 (1999), pp. 44–56. issn: 0304-8853. doi: https://doi.org/10.1016/S0304-8853(99)00397-2.

[2] Jan-Ulrich Thiele, Stefan Maat, and Eric E. Fullerton. “FeRh/FePt exchange spring films for thermally assisted magnetic recording media”. In: *Applied Physics Letters* 82.17 (2003), pp. 2859–2861. issn: 0003-6951. doi: 10.1063/1.1571232. url: https://doi.org/10.1063/1.1571232%20https://aip.scitation.org/doi/pdf/10.1063/1.1571232.

[3] Rudolf Gross and Achim Marx. *Festkörperphysik*. 2014. isbn: 978-3-11-035869-8. doi: 10.1524/9783110358704. url: https://www.degruyter.com/view/product/278639.

[4] Wolfgang Nolting. *Grundkurs Theoretische Physik 6*. 2014. isbn: 978-3-642-25392-8. doi: 10.1007/978-3-642-25393-5.

[5] M. Farle. “Ferromagnetic resonance of ultrathin metallic layers”. In: *Rep. Prog. Phys.* 61 (1998), p. 755.

[6] Sergej V. Vonsovskij and Dirk Ter Haar. *Ferromagnetic resonance : the phenomenon of resonant absorption of a high-frequency magnetic field in ferromagnetic substances*. 1. Engl. ed. International series of monographs in solid state physics. Oxford [u.a.]: Pergamon Press, 1966.

[7] Harald Ibach and Hans Lüth. *Festkörperphysik*. 2009. isbn: 978-3-540-85794-5. doi: 10.1007/978-3-540-85795-2.

[8] Kilian Lenz. “Magnetische Anisotropie und Dämpfungsmechanismen in ultradünnen 3d-Ferromagneten: eine FMR-Studie”. Thesis. 2005.

[9] Michael Körner. “Morphology-Induced Magnetic PhenomenaStudied by BroadbandFerromagnetic Resonance”. Thesis. 2013.

[10] C. Kittel. “ON THE THEORY OF FERROMAGNETIC RESONANCE ABSORPTION”. In: *Physical Review* 73.2 (1948), pp. 155–161. issn: 0031-899X. doi: 10.1103/PhysRev.73.155. url: %3CGo%20to%20ISI%3E://WOS:A1948UB29300008.

[11] T. L. Gilbert. “A phenomenological theory of damping in ferromagnetic materials”. In: *IEEE Transactions on Magnetics* 40.6 (2004), pp. 3443–3449. issn: 0018-9464. doi: 10.1109/TMAG.2004.836740. url: https://ieeexplore.ieee.org/ielx5/20/29738/01353448.pdf?tp=&arnumber=1353448&isnumber=29738&ref=.

[12] J. H. E. Griffiths. “Anomalous High-frequency Resistance of Ferromagnetic Metals”. In: *Nature* 158.4019 (1946), pp. 670–671. issn: 1476-4687. doi: 10.1038/158670a0. url: https://doi.org/10.1038/158670a0%20https://www.nature.com/articles/158670a0.pdf.

[13] B. W. Zingsem. “A theory of the magnetodynamic response function”. Thesis. 2016.

[14] Ralph T. Weber. *ELEXSYS II E 500 User's Guide*. 2013.

[15] Eric W. Weisstein. "Cauchy Distribution." In: (). url: http://mathworld.wolfram.com/CauchyDistribution.html.

[16] Volodymyr Popovych et al. "Dyson line and modified Dyson line in the EPR measurements". In: *Nukleonika* 60.3 (2015), pp. 385–388.

[17] A. Heidarian et al. "Ferromagnetic resonance of MBE-grown FeRh thin films through the metamagnetic phase transition". In: *Physica Status Solidi B-Basic Solid State Physics* 254.10 (2017), p. 7. issn: 0370-1972. doi: 10.1002/pssb.201700145. url: %3CGo%20to%20ISI%3E://WOS:000412897900021.

[18] P. J. Kelly and R. D. Arnell. "Magnetron sputtering: a review of recent developments and applications". In: *Vacuum* 56.3 (2000), pp. 159–172. issn: 0042-207X. doi: https://doi.org/10.1016/S0042-207X(99)00189-X.

[19] Anna Semisalova. unpublished.

[20] S. Cervera et al. "Modulating the phase transition temperature of giant magnetocaloric thin films by ion irradiation". In: *Physical Review Materials* 1 (2017). doi: 10.1103/PhysRevMaterials.1.065402. url: https://journals.aps.org/prmaterials/pdf/10.1103/PhysRevMaterials.1.065402.

[21] J. S. Kouvel. "Unusual Nature of the Abrupt Magnetic Transition in FeRh and Its Pseudobinary Variants". In: *Journal of Applied Physics* 37.3 (1966), pp. 1257–1258. issn: 0021-8979. doi: 10.1063/1.1708424. url: https://doi.org/10.1063/1.1708424%20https://aip.scitation.org/doi/pdf/10.1063/1.1708424.

[22] A. Heidarian et al. "Tuning the antiferromagnetic to ferromagnetic phase transition in FeRh thin films by means of low-energy/low fluence ion irradiation". In: *Nuclear Instruments and Methods in Physics Research Section B: Beam Interactions with Materials and Atoms* 358 (2015), pp. 251–254. issn: 0168583X. doi: 10.1016/j.nimb.2015.06.027.

[23] Nao Fujita et al. "Magnetic states controlled by energetic ion irradiation in FeRh thin films". In: *Journal of Applied Physics* 107.9 (2010), 09E302. issn: 0021-8979. doi: 10.1063/1.3359440. url: https://doi.org/10.1063/1.3359440%20https://aip.scitation.org/doi/pdf/10.1063/1.3359440.

[24] Nao Fujita et al. "Effects of energetic heavy ion irradiation on the structure and magnetic properties of FeRh thin films". In: *Nuclear Instruments and Methods in Physics Research Section B: Beam Interactions with Materials and Atoms* 267.6 (2009), pp. 921–924. issn: 0168-583X. doi: https://doi.org/10.1016/j.nimb.2009.02.054.

[25] Fallot M. R. and Hocart. In: *Rev. Sci. 77 498* (1939).

[26] J. M. Lommel and J. S. Kouvel. "Effects of Mechanical and Thermal Treatment on the Structure and Magnetic Transitions in FeRh". In: *Journal of Applied Physics* 38.3 (1967), pp. 1263–1264. issn: 0021-8979. doi: 10.1063/1.1709570. url: https://doi.org/10.1063/1.1709570%20https://aip.scitation.org/doi/pdf/10.1063/1.1709570.

[27] de Bergevin F L and Muldawer. In: *C. R. Acad. Sci. 252 1347* (1961).

[28] J. S. Kouvel and C. C. Hartelius. "Anomalous Magnetic Moments and Transformations in the Ordered Alloy FeRh". In: *Journal of Applied Physics* 33.3 (1962), pp. 1343–1344. issn: 0021-8979. doi: 10.1063/1.1728721. url: https://doi.org/10.1063/1.1728721%20https://aip.scitation.org/doi/pdf/10.1063/1.1728721.

[29] C. Koenig. “Self-consistent band structure of paramagnetic, ferromagnetic and antiferromagnetic ordered FeRh”. In: *Journal of Physics F: Metal Physics* 12.6 (1982), pp. 1123–1137. issn: 0305-4608. doi: 10.1088/0305-4608/12/6/013. url: http://dx.doi.org/10.1088/0305-4608/12/6/013%20https://iopscience.iop.org/article/10.1088/0305-4608/12/6/013/pdf.

[30] E. Mancini et al. “Magnetic phase transition in iron-rhodium thin films probed by ferromagnetic resonance”. In: *Journal of Physics D-Applied Physics* 46.24 (2013), p. 5. issn: 0022-3727. doi: 10.1088/0022-3727/46/24/245302.

[31] Jiangwei Cao et al. “Magnetization behaviors for FeRh single crystal thin films”. In: *Journal of Applied Physics* 103.7 (2008), 07F501. issn: 0021-8979. doi: 10.1063/1.2828812. url: https://doi.org/10.1063/1.2828812%20https://aip.scitation.org/doi/pdf/10.1063/1.2828812.

Danksagung

Ich möchte mich bei Prof. Dr. rer nat. Michael Farle bedanken, der es mit ermöglichte diese Arbeit zu schreiben und eigenständige Messungen durchzuführen.

Ebenso herzlichen Dank gebührt Dr. Anna Semisalova, die mich bei der Reise in die magnetische Anisotropie und der ferromagnetischen Resonanz tatkräftig durch ausführliche Erklärungen unterstützt hat.

Zudem möchte ich mich bei Dr. Ralf Meckenstock und Dr. Detlef Spoddig für die Diskussionen, Interpretationen und Hilfe beim Aufbau der Experimente bedanken.

Ich bedanke mich ebenso bei Benjamin Zingsem und Nicolas Josten, für die Einleitung und Hilfestellungen in die Computer gestützte Analyse der Messdaten.

Ebenso möchte ich mich bei Dr. Mustafa Tokaç für die sehr gute Zusammenarbeit bedanken.

Außerdem möchte ich bei dem Rest der Arbeitsgruppe Farle für eine sehr freundliche Atmosphäre und interessante Diskussionen bedanken.

Mein Dank geht ebenso an die Arbeitsgruppe um Prof. Dr. Tom Thompson der Universität Manchester für die Herstellung der FeRh Dünnfilme, genauso wie das Ion Beam Center im Helmholtz Zentrum Dresden Rossendorf für die Neon-Ionen Bestrahlung und RBS Messungen der FeRh Proben.

Selbstständigkeitserklärung

Hiermit erkläre ich, Jonas Wiemeler, dass ich die vorliegende Arbeit selbstständig angefertigt und keine anderen als die angegebenen Hilfsmittel verwendet habe. Sämtliche wissentlich verwendete Textausschnitte, Zitate oder Inhalte anderer Verfasser wurden ausdrücklich als solche gekennzeichnet.

Ort, Datum

Unterschrift